Developing a Quantum Toolbox: Experiments with a Single-Atom Harmonic Oscillator and Prospects for Probing Molecular Ions

David A. Lane

Advisor: Professor David A. Hanneke
April 27, 2017

Submitted to the
Department of Physics and Astronomy
of Amherst College
in partial fulfillment of the
requirements for the degree of
Bachelor of Arts with honors

Abstract

Many extensions to the Standard Model predict that the fundamental constants of nature exhibit time variation. We propose using high precision measurements of the vibrational and rotational energy levels of homonuclear diatomic molecular ions to perform a model-independent search for time variation in the proton-to-electron mass ratio μ. We have shown that a precision measurement of two accidentally degenerate levels in $^{16}{O_2}^+$ is capable of increasing the present bounds on variation in μ by a factor of $10 - 100$. Preparing the internal state of $^{16}{O_2}^+$ is complicated by its many degrees of freedom. We will use quantum logic spectroscopy (QLS) to manipulate and probe this molecule's state. We will trap $^{16}{O_2}^+$ in a linear Paul trap with a $^9Be^+$ ion and couple the molecule's internal states to its motion, which is shared with the co-trapped $^9Be^+$. Understanding the motion of $^9Be^+$ in the trap is necessary to prepare and interpret the results of this experiment. This thesis focuses both on the theoretical underpinnings of our proposed experiment and on building the foundation for performing QLS.

We identify the molecular properties which make certain molecules promising for high precision measurements of μ variation. Molecules with deep potential wells tend to be maximally sensitive to changes in μ and those with closely-spaced vibrational levels should be easier to measure. Experiments on N_2, Cl_2, Br_2, and ${I_2}^+$ should have an absolute sensitivity to variation in μ on the same order of magnitude as our proposed experiment on $^{16}{O_2}^+$.

Furthermore, we investigate the motion of a single trapped $^9Be^+$ ion in our linear Paul trap to prepare for future QLS experiments. We parameterize the electric potential experienced by trapped ions. By modulating the axial trapping potential and measuring the system's resonant frequencies, we identify these parameters and thereby fully characterize the motion of trapped $^9Be^+$. The techniques employed in these experiments can be used to identify an ion co-trapped with $^9Be^+$ by treating the system as a coupled oscillator. We show how the axial modes of the $^9Be^+ - ^9Be^+$ system could be distinguished from those of the $^9Be^+ - BeH^+$ system, which would confirm that our system can identify trapped ions based on resonance shifts of a few kHz. Finally, we briefly turn our attention to the properties of the $^9Be^+ - {}^{16}{O_2}^+$ system and discuss the next steps in preparing to make our QLS experiments.

Acknowledgements

Many seniors I have met over my years at Amherst College have spoken in dark tones of the dreaded senior year, dominated by the foreboding thesis and its induced sleepless nights of stress. I have found my own journey to be quite different, primarily thanks to the guidance, organization, and helpfulness of Professor David Hanneke. Instead of months dominated by stress, I have found myself continually inspired by him, continually propelled by excitement down this path of learning and scientific apprenticeship. It was challenging and memorable, but always accessible. Thank you, Professor Hanneke, for fielding my many (often repetitive) questions throughout the year, for teaching me laboratory techniques, and guiding me through the research process. You have been an incredible mentor and have made this a great and rewarding adventure, one that I am so thankful to have taken.

I would also like to thank Ryan Carollo, without whom I would have been lost amid the laser system. He selflessly shared his wisdom and knowledge with me, and has been ever patient and helpful as I cultivated proficiency in the lab.

The faculty and staff of the Department of Physics and Astronomy have been essential to my growth as a person and as a physicist. To those of you

with whom I took classes, thank you for your continued support over the years. To all of you, as well as my fellow physics majors, thank you for providing a supportive atmosphere and four years of challenges, laughs, and smiles.

This material is based upon work supported by the Amherst College Dean of the Faculty and by the National Science Foundation under CAREER Grant No. PHY-1255170. I could not have performed my research without this support.

Contents

List of Figures

Chapter 1

Introduction

Few discoveries would motivate us to reimagine the basic qualities of our reality like witnessing a change in one of the fundamental constants of nature. These constants give rise to the universe as we experience it; the Standard Model of particle physics is constructed with these immutable constants at its core. If we observe one of these constants exhibiting time-variance, the field of particle physics would experience a monumental paradigm shift as now-extraneous theories of reality would need to be appended to the Standard Model to account for the discovery.

This thesis presents research that should help future researchers in Professor Hanneke's laboratory make a high precision measurement of one such fundamental constant: the proton-to-electron mass ratio $\mu = m_p/m_e$. I have contributed to our understanding of the powerful and versatile apparatus that should make this precision measurement achievable. In particular, my research focuses on how this apparatus can be used to manipulate atoms and molecules

in spectroscopy experiments which yield precise information about the time variation of μ.

With this goal in mind, it is with utmost enthusiasm that I offer to take you with me on this journey of scientific discovery.

1.1 A Quest for the Unknown

Attempting to precisely measure the time variation of fundamental constants has been a field of active research since 1937, when Paul Dirac speculated that certain constants might not have fixed values, but vary with the age of the universe [1]. The time variation of constants such as the fine structure constant, the gravitational constant, the cosmological constant, and the proton-to-electron mass ratio would have a profound effect on our understanding of the laws of nature. There is a particularly interesting result that emerges from a nonzero variation in μ. Since the electron's mass is determined by the strength of the electroweak force and the proton's mass is tied to the strength of strong force interactions, such a change would indicate a relative change in the strength of these two forces over time. The exact consequences of this variation, and equivalently, variation in μ, are important insofar as they are predicted by many extensions to the Standard Model.

For example, theories that predict the existence of higher dimensions in an effort to unify the fundamental forces of nature (such as Kaluza-Klein and superstring theories) postulate that, through its relationship to the relative strengths of these forces, the fundamental parameter μ is constant when con-

sidered in all dimensions, but its projections in any lower-dimensional space should change with the shape and evolution of these dimensions; the effective four-dimensional value would vary [2]. These theories each postulate particular shapes and time-evolutions of additional spacetime dimensions, and thus different rates of variation of μ. Thus emerges the theoretical impetus for measuring precise changes in μ: As we make increasingly precise measurements of this ratio, we can begin discarding theories that predict different rates of change and come closer to identifying extensions to the standard model that are based in experimental evidence; it is a path to discovering a unified theory.

Our lab will search for fractional changes in μ by measuring the energy differences between two closely spaced molecular vibrational states of different electronic energy levels. Generally, the energies of these states are sensitive to changes in μ, particularly if these two states are nearly degenerate [3, 4]. Our lab will use an oxygen molecular ion ($^{16}O_2{}^+$) to make our measurements of μ, due to a few useful properties of its molecular structure and energy level spacing. I will discuss this choice and the theoretical underpinnings of this decision in Chapter 2, where I will also introduce other potentially useful molecules.

1.2 Quantum Logic Spectroscopy

Molecules such as $^{16}O_2{}^+$ exhibit more complex physical phenomena than atoms due to their rotational and vibrational degrees of freedom. Although these degrees of freedom are the source of molecular μ-dependence, they make

molecules problematic to manipulate. Specifically, the internal states of oxygen we wish to study are difficult to prepare and oxygen's transitions make it unsuitable for laser cooling. To overcome these challenges, our lab will employ a general technique known as Quantum Logic Spectroscopy (QLS) [5], using an ion trap to confine the motion of positively charged particles to a small region of space which can be easily studied and controlled.

In our case, QLS involves trapping an atomic ion (the logic ion) alongside $^{16}O_2{}^+$ (the spectroscopy ion). The key to QLS is that the internal state of either ion can be coupled to its motion, which is shared via the Coulomb force. When the motion is coupled, preparing a specific state in the spectroscopy ion is equivalent to preparing a corresponding state in the logic ion. The logic ion acts as a probe to both prepare and detect the internal states of the molecule. To be effective, the logic ion should be easy to cool and its internal states should have a high detection efficiency. Conveniently, this technique bypasses the difficulty of manipulating or detecting the molecule directly.

One of the many advantages of this technique is its versatility. As long as our ion trap is able to simultaneously trap both an $^{16}O_2{}^+$ molecule and a logic ion, we do not need to develop a system specifically designed to manipulate oxygen; instead, we can design the apparatus to cool and detect a particular species of logic ion, and rely on the coupled motion of this ion and $^{16}O_2{}^+$ to perform our experiments. Such a setup allows us to easily exchange the molecule we wish to study without dismantling our ion trap or laser system.

Our lab uses beryllium ($^9Be^+$) as the logic ion, since it has easily driven transitions and can be efficiently cooled. Its properties in such experiments

are well-documented [5, 6].

1.3 The Apparatus

Above, I have described the end goal of this lab's experiments and the general technique we will use to collect data. Before we can perform these exciting QLS experiments, however, we need a laboratory setup capable of cooling and manipulating the states of trapped ions. This section describes the apparatus built by many members of this lab over the past few years and how it can be used to accomplish our lab's goal. Our apparatus consists of an ion trap used to confine the logic and spectroscopy ions and an optics system designed to tune a laser to particularly useful frequencies for manipulating the states of beryllium.

1.3.1 Ion Trapping

The purpose of our ion trap is to confine ions to a specific region of space and make trapped ions move in well-understood ways. This will allow for easy manipulations of their motion and thus their internal states and energy. Our work has been performed on ions trapped in a linear Paul trap located in an ultra-high vacuum. These traps are created by applying a combination of static and dynamic electric fields to electrodes, arranged in such a way to create a minimum in the potential field in the center of the trap. Effectively, a trapped ion sees a superposition of two potentials which together yield a three-dimensional saddle-shaped potential energy landscape.

The first potential, created by the dynamic fields, oscillates with a high enough frequency to keep ion motion confined to the center of the trap by inverting this saddle shape (Fig. 1.1); this component is responsible for the curvature and time-dependence of the saddle shape. If we define the potential energy of an ion in the trap such that at the center of the trap the ion has no potential energy, we can treat this potential as quadratic, since the leading term in a Taylor expansion of the potential about the equilibrium point is the second-order term.

Controlled entirely by electrostatic charge distributions, the second potential provides trapping in the third dimension (defined as the axial dimension), and this potential can likewise be considered quadratic. This component confines particles to the surface of this saddle shape. By design, ions are more weakly trapped in this dimension than in the others. This causes trapped ions to spread out in a chain along the z-axis. Since we can control the axial component of the potential independently of the other components, we can easily manipulate the axial motion of the ions using principles of classical mechanics to treat this system as a coupled harmonic oscillator in the axial dimension. Thus, we can easily analyze and control the motion of trapped ions, which will allow us to perform QLS experiments. I will discuss the theory behind linear Paul traps in more detail in the context of trapped ion motion and resonances in Chapter 3.

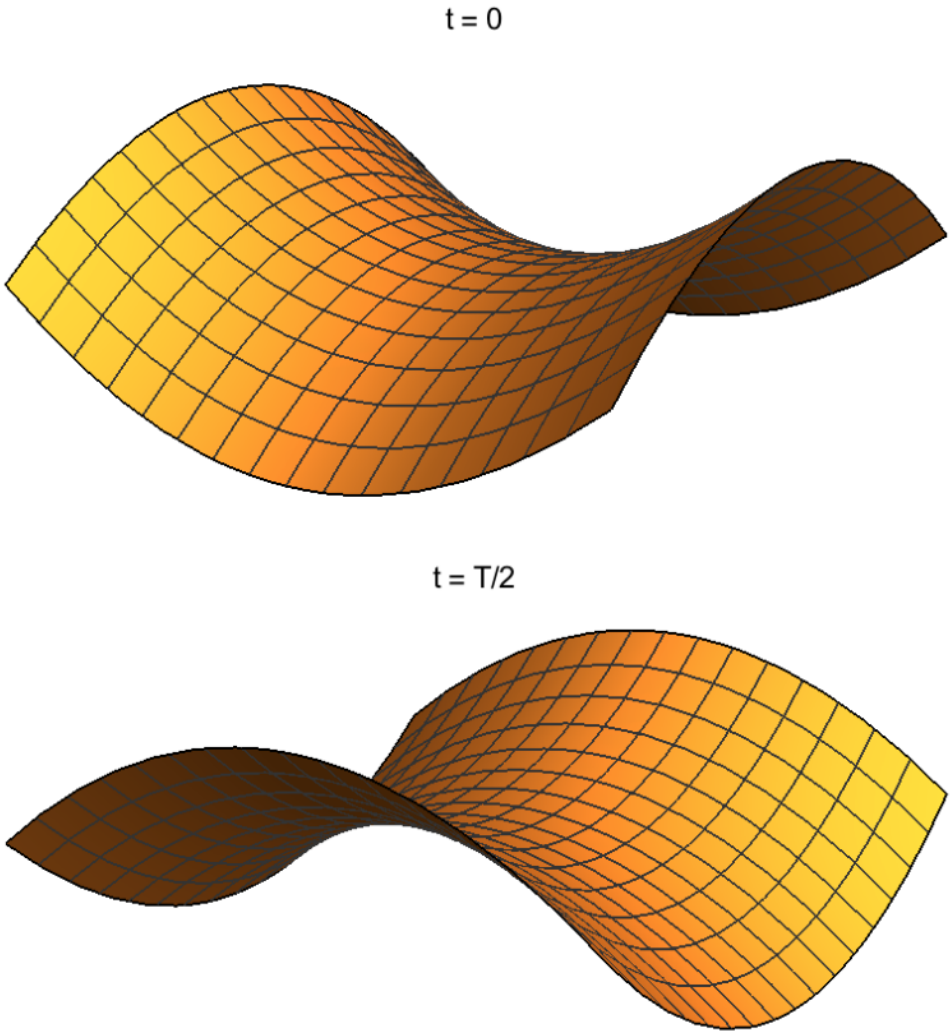

Figure 1.1: Saddle-shaped Potential of a Paul Trap. This illustration shows the saddle-like potential landscape created by a Paul trap's static and dynamic electric potentials. The dynamic contribution to this potential oscillates at a well-known frequency, causing the saddle to invert once every half period. If the frequency of oscillation is high enough, a particle in this potential will be confined to the center of the saddle.

1.3.2 Laser Cooling

In order to prepare a known state of a trapped $^{16}O_2{}^+$ molecule, we must be able to cool the co-trapped $^9Be^+$ to an appropriate low-energy state. This is accomplished by exploiting the Doppler shift of excited ions in a technique known as Doppler cooling. An atom struck by a photon with an energy corresponding to one of the atom's electronic energy levels will absorb the photon, causing a change in the atom's momentum equal to the momentum of the photon. The photon will later be emitted in a random direction, causing a corresponding change to the atom's momentum. Now, imagine the frequency of the incident photon corresponds not to the exact energy of the transition, but to a slightly lower energy (that is, it is detuned to a redder frequency). The atom is more likely to absorb such detuned photons from a laser beam if the atom has a velocity directed toward the photon source, since from the atom's reference frame, the Doppler effect will blueshift the beam, effectively bringing it closer to resonance. Conversely, if the atom is traveling in the same direction as photons from the source, the light will appear redshifted to the atom, effectively shifting the beam's frequency further from the atom's resonance. Thus, if a detuned beam is incident on an atom, the atom will more often absorb photons moving opposite its direction of travel and, therefore, its momentum will decrease. This ultimately reduces its thermal velocity, cooling the atom.

The random changes to the atom's velocity resulting from the later emission of the photon do not prevent the cooling (since the average of these changes results in no net change in momentum), but they do limit it. The atom

will spontaneously emit one photon per natural lifetime of the excited state, effectively causing the atom to undergo a random walk at a rate equal to the natural linewidth γ of the excited state. This limiting motion is associated with the atom's minimum temperature, known as the Doppler temperature, which is defined by

$$k_B T_D \equiv \frac{\hbar\gamma}{2}, \tag{1.1}$$

where k_B is Boltzmann's constant and $\hbar$ is the reduced Planck constant [7]. Our lab uses the transition $^2S_{1/2} \leftrightarrow {}^2P_{3/2}$ in $^9Be^+$ for Doppler cooling, which has a linewidth of $\gamma/(2\pi) = 19.4$ MHz and thus a Doppler temperature of $T_D = 466$ μK.

The experiments I describe in Chapter 3 rely on classical phenomena of trapped ions. These experiments only require that trapped beryllium ions are cool enough that their thermal motion is localized on the scale of the ion trap such that they can be seen as crystals with radii of a few μm, not blurs. As such, my experiments were performed using only Doppler cooling.

However, QLS experiments use motion to transfer information, so minimizing the ions' thermal motion maximizes the fidelity of the information. To perform QLS, we will want to cool beryllium ions below the Doppler limit (and ideally, to their motional ground state). Resolved sideband cooling accomplishes this cooling. This process uses two lasers to stimulate emission which lowers the atom's hyperfine state without affecting its motional state. We tune the first laser to the transition from the S state's $F = 1$ level to an energy slightly below the P state (detuned by GHz), and the second laser to the transition from the S state's $F = 2$ state to the same energy. When

these lasers are incident on beryllium, ions in the $|S, F = 1\rangle$ state will absorb a photon from the first laser and immediately emit a photon with an energy corresponding to that of the second laser via stimulated emission. Instead of electronically exciting the atom to the P state, these lasers bring the atom to a different hyperfine state in the same electronic energy level. This is called a stimulated Raman transition and is discussed in the context of cooling beryllium atoms in Refs. [5, 8, 9]. This process should be able to bring $^9Be^+$ to the ground state.

1.3.3 Frequency Preparation

In conclusion, the apparatus must be able to output five ultraviolet wavelengths to cool and perform experiments on $^9Be^+$. We need two resonant beams, one for each hyperfine state of the $^2S_{1/2} \leftrightarrow {}^2P_{3/2}$ transition. The beam tuned to the $F = 1$ state is a repump beam that, via a transition to the P state, returns atoms to the $F = 2$ state. The beam tuned to the $F = 2$ state is the (slightly red-detuned) resonant beam that is used for Doppler cooling. Because it causes spontaneous emission of photons, the resonant beam can be used to detect the ions on a photomultiplier tube or camera. The third beam is a detuned beam with an energy between both hyperfine transitions. Since it is far from resonance, the detuned beam only excites transitions in very hot ions and is unable to bring trapped $^9Be^+$ close to the Doppler limit. It is, however, very effective at cooling ions from room temperature to temperatures suitable for detection and Doppler cooling with the resonant beam. The other two beams drive the stimulated Raman transitions. The experiments I discuss

in Chapter 3 use the detuned beam to cool ions and the resonant beam to detect them.

We create these beams by preparing one laser at approximately 313 nm via third-harmonic generation (a multistep process described below), which we then send through an appropriate modulator to tune it precisely to the desired frequency. Our setup uses acousto-optic modulators (AOMs) to accomplish the fine tuning of the UV light. AOMs diffract and shift the frequency of light via the acousto-optic effect, whereby a mechanical strain on a material changes its permittivity [10]. In an AOM, sound waves are the source of this mechanical stress. When incoming light passes through this material, it is diffracted and experiences a frequency shift equal to the frequency of the acoustic wave. In our setup, we send the UV beam through a series of AOMs corresponding to the frequencies in which we are interested. If we turn on one AOM, it will shift the frequency appropriately and diffract the beam. We then send this diffracted beam through the center of the trap.

Since these modulators accomplish the fine-tuning, all we need to manipulate beryllium ions is a single laser that can output a UV frequency around 313 nm consistently at a sufficient power. Unfortunately, generating light at this wavelength is not straightforward. No such laser is readily accessible because few available semiconductors have optical gain at this wavelength [11, 12]. Thus, we need to employ nonlinear optics to alter the frequency of a source laser to the desired frequency. Two nonlinear optical phenomena are particularly useful in our setup: second-harmonic generation (SHG) and sum-frequency generation (SFG). In SHG, a source laser is doubled in frequency as

it passes through a particular nonlinear media. Effectively, identical photons from the source are combined, resulting in photons of twice the energy (and hence, twice the frequency). Similarly, in SFG, two sources are combined, yielding output light which has a frequency equal to the sum of the sources' frequencies.

It has been shown that, via SHG, a dye laser emitting at 626 nm can effectively be used to cool $^{9}Be^{+}$ ions [13]. However, for purposes of balancing efficiency, power, and cost [11], our lab uses an external cavity diode laser (ECDL), emitting at 940 nm, as a source. Through a combination of SHG and SFG, we can generate light at the desired UV frequency. The ECDL frequency is doubled via SHG, yielding blue light with a wavelength of 470 nm, which is then summed via SFG with the light at 940 nm, resulting in light with a wavelength of 313 nm. Since we have effectively tripled the frequency of the source, this is called third-harmonic generation (THG). The entire laser system is illustrated in Fig. 1.2. It can be roughly broken into four steps.

The first two steps directly affect the infrared ECDL source. Some of the light is diverted to a Fabry-Pérot cavity to be referenced against a helium-neon laser to stabilize the ECDL. This step was implemented and tested by Chu Cheyenne Teng [14]. A beam splitter separates some of this IR light and directs it toward the SHG cavity, while the rest skips the SHG step, since it will be used in the SFG step. Both beams are sent through tapered amplifiers designed to raise their powers to levels that can, after the power loss involved in THG, effectively perform cooling and internal state control of trapped beryllium. The tapered amplifier's design and specifications are

discussed by Edward Kleiner [8]. Both the SHG and SFG steps occur in cavities which are designed to pass the incoming laser through a nonlinear material many times (via precise alignment of mirrors) to build up output power. Without this buildup, only a small fraction of light at the altered frequency would be created in these processes.

For second-harmonic generation, we initially used the crystal bismuth triborate (BiBO, BiB_3O_6) as the nonlinear material for frequency conversion, but eventually replaced it with lithium triborate (LBO, LiB_3O_5) to improve stability. BiBO is particularly useful due to its high nonlinear coefficient which results in a high conversion efficiency in this process [15]. However, at the high end of our operating power, BiBO experienced photorefractive damage which severely diminished the magnitude and stability of the converted light over timescales of tens of minutes. Since the limitations of BiBO and the nature of this photorefractive damage are not well-documented, I collected information related to BiBO's performance in the context of SHG, which I discuss in Appendix A. I hope this information is useful to those studying materials science and optics, but its performance was inadequate for the purposes of our THG setup. Thus, we use LBO as a nonlinear crystal for SHG instead. With a lower nonlinear coefficient, LBO produces less blue light for a given IR input than BiBO, but experiences none of the same damage as BiBO at high operating powers. Because it can withstand higher operating powers, we can produce higher power stable blue light with LBO than with BiBO.

The blue light from the SHG cavity is combined with the earlier split infrared light to produce UV in the sum-frequency generation step. We use

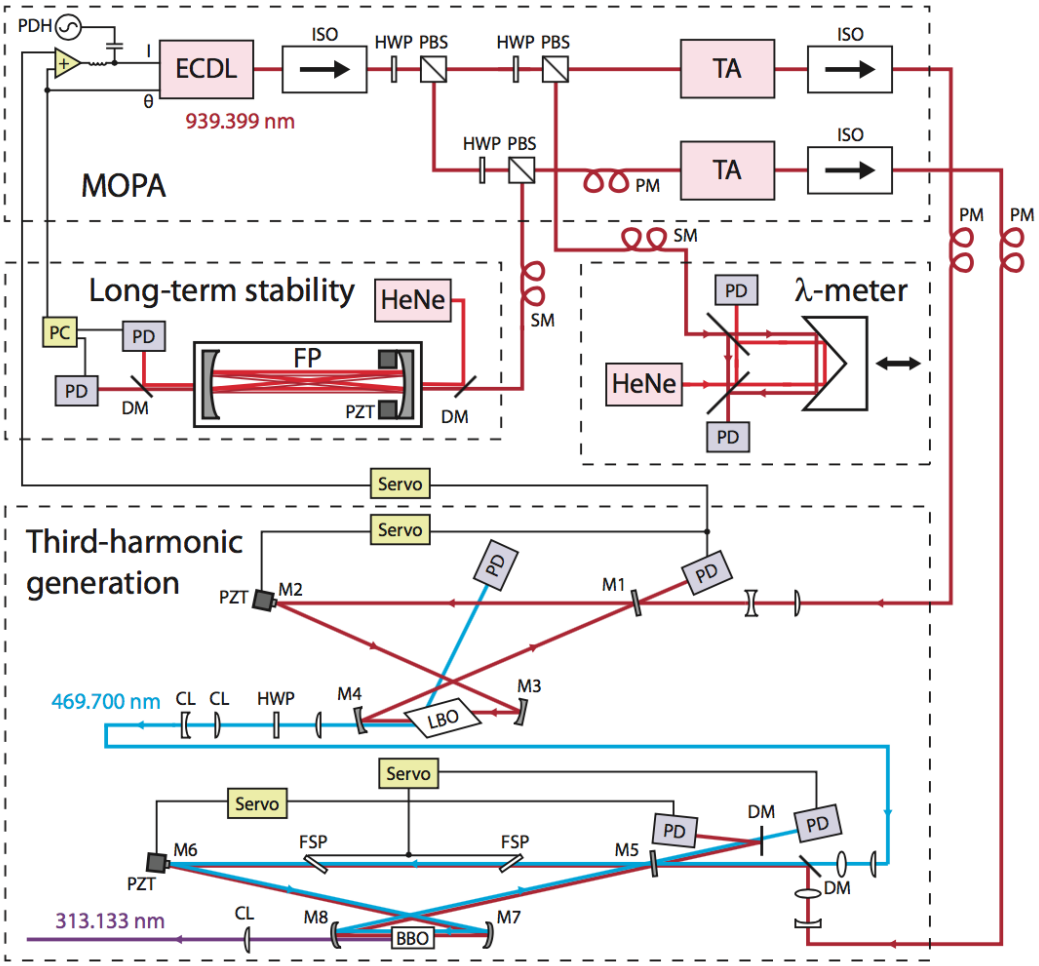

Figure 1.2: Hanneke Lab THG Laser System. The main components include the external cavity diode laser (ECDL), the tapered amplifier (TA), the stable helium-neon reference laser (HeNe) in the Fabry-Pérot (FP) cavity, the LBO crystal responsible for second-harmonic generation, and the BBO crystal responsible for sum-frequency generation. This is from Ref. [11], where the other elements of the system are discussed more completely.

β-barium borate (BBO, BaB_2O_4) as the nonlinear crystal for this process.

As discussed in Ref. [11], this THG system can output approximately 36 mW of 313 nm light with power variations under 10% over the course of one day. Its typical output is $5 - 10$ mW, which is sufficient to perform the experiments discussed in Chapter 3.

1.4 Developing a Quantum Toolbox

This laser system's true strength is its versatility, as it is able to cool and manipulate the internal states of trapped $^9Be^+$ ions by turning on particular AOMs in a sequence of pulses. By programming a pulsing procedure, we can perform measurements on cooled beryllium ions, effectively allowing us to begin developing a toolbox of information and techniques for manipulating our logic ion. This is the overarching goal of my research. With this information in hand, our lab can delve into QLS experiments and probe the time variation of the proton-to-electron mass ratio.

The first element of this toolbox is a theoretical one, not related to the logic ion itself, but to oxygen, our spectroscopy molecule. As I mentioned briefly in Sect. 1.1, degenerate vibrational states in $^{16}{O_2}^+$ are sensitive to time variation of μ. However, our choice of oxygen as the molecule we use to detect these changes is, though informed by molecular theory, somewhat arbitrary. I will start furnishing this quantum toolbox in Chapter 2 by discussing what other molecules might be useful in this QLS experiment. My aim is twofold: determine to what extent oxygen's sensitivity to variation in μ is unique, and

provide a list of compelling alternative spectroscopy ions which can serve to extend and support the experiments our lab performs on oxygen.

The bulk of my work has been experimental, directly related to the properties of our linear Paul trap and how the $^9Be^+$ logic ion behaves in the trapping field. As I mentioned in Section 1.2, QLS experiments rely on a transfer of information, encoded in classical motion and quantum internal states, from the spectroscopy ion to the logic ion and vice versa. Chapter 3 focuses on decoding the classical motion of trapped beryllium, so we can easily manipulate its movement (and thus the movement of co-trapped oxygen) in the trap. This involves solving and parameterizing the system's equations of motion. I approximate the trapping potential as harmonic and use the trap's resonant frequencies to find the values of parameters which appear in the electric potentials experienced by trapped ions. Armed with this information, I prepare for QLS experiments by demonstrating the precision required for my resonance-based analysis to identify co-trapped ions.

Chapter 2

Precision Measurements with Diatomic Molecules

Both cosmological and laboratory spectroscopy experiments have attempted to detect changes in μ over time. These experiments do not measure a specific change, but instead they place a bound on the maximum possible time variation, which is smaller in systems with less systematic error. The smallest laboratory bound on variation in μ, measured as $\dot{\mu}/\mu$, is on the order of 10^{-16} yr^{-1}, found from atomic clock experiments which rely on hyperfine measurements of cesium atoms [16, 17]. Therefore, these experiments require a model of how the nucleon mass affects nuclear magnetic moment to yield a precise measurement of μ.

In comparison, our method is model-independent, since we will directly observe the inertial mass in motion. We will use the vibrational and rotational energy levels of oxygen molecules to detect changes in μ. While the

bounds on such molecular measurements of $\dot{\mu}/\mu$ are currently larger than atomic clock measurements, a number of studies have shown precision molecular spectroscopy experiments to be promising for tightening the bounds on variation in μ [3, 4, 18–20]. In particular, DeMille *et al.* [3] proposed that these experiments in Cs_2 could potentially measure a fractional variation in μ on the order of 10^{-17}.

As discussed in our lab's recent publication [4], our experimental procedure using $^{16}O_2{}^+$ has the potential to increase the present bounds on variation in μ by a factor of $10 - 100$. In this chapter, I briefly summarize why our QLS experiments with $^{16}O_2{}^+$ are capable of such precision. I explain why molecular spectroscopy is promising and why $^{16}O_2{}^+$ is particularly sensitive to variation in μ. Additionally, I expand upon our discussion in Ref. [4] by presenting other molecules that might be useful in similar spectroscopy experiments due to their similarly high absolute sensitivity to this variation.

2.1 Molecular Potential Wells

Molecular sensitivity to variation in μ results from the mass-dependence of its energy levels. Thus, understanding the shape of a particular molecule's potential energy curve allows us to investigate the experimental viability of the molecule. This section explains how these potential wells are shaped and introduces the parameters and equations which will be referenced in the following sections to explain how sensitivity to μ arises.

A diatomic molecule's vibrational potential energy varies as its internuclear

distance changes. This relationship is approximately harmonic over small oscillations about equilibrium, but diverges from the behavior of a harmonic oscillator far from equilibrium. As the two nuclei approach each other, the Coulomb repulsion between them brings the system's energy toward infinity. As the internuclear distance becomes large, the Coulomb attraction responsible for the atoms' bond weakens, so the system's potential energy asymptotes to zero (assuming the convention of bound atoms having negative potential energies). We can describe this anharmonic behavior as a perturbation of a single-particle harmonic oscillator with a mass equal to the reduced mass of the two-atom system.

The potential energy of a single-particle harmonic oscillator is proportional to the square of the particle's distance from equilibrium $q = r - r_e$. We can generally model anharmonicity by adding terms with higher-order dependence on q with coefficients much smaller than that of the second order term. For a quantum mechanical system, the energy eigenstates of this anharmonic potential are the solutions of the Schrödinger equation.[1] The resulting energy eigenstates are typically parameterized with a set of molecular constants ω_e, $\omega_e x_e$, $\omega_e y_e$, etc. with units of inverse wavelength [21]. The energies are

$$E_\nu/(hc) = \omega_e(\nu + \tfrac{1}{2}) - \omega_e x_e(\nu + \tfrac{1}{2})^2 + \omega_e y_e(\nu + \tfrac{1}{2})^3 + ... \qquad (2.1)$$

where ν is the vibrational quantum number ($= 0, 1, 2...$), h is Planck's constant, c is the speed of light, and the molecular constant appearing in each successive term is much smaller than the one appearing in the term before it [22]. Unlike

[1] This is a phenomenological model, not a first principles description.

the harmonic oscillator, the energy levels of the anharmonic oscillator are not evenly spaced: they grow closer together as ν increases. Often, it is convenient to express energies in units of wavenumber (inverse wavelength), accomplished by dividing energy by hc, so I will group this factor under relevant energies throughout this section for ease of conversion.

The Morse potential, an approximation of the potential energy of a diatomic molecule, provides a means of equating measured values of the term coefficients in Eq. 2.1 to characteristic quantities of the molecule. This gives us a means of solving for these coefficients or characteristic quantities and allows us to easily calculate the vibrational energy levels. For a given internuclear distance r, the Morse potential is

$$U(r) = D_e[1 - e^{-\beta(r-r_e)}]^2, \tag{2.2}$$

where D_e is the depth of the potential energy well, defined by the difference in energy between the bottom of the potential well and the energy of the dissociated atoms ($r = \infty$), r_e is the equilibrium bond distance, and β is a constant with units of inverse length which controls the width of the potential well [21]. Substituting this expression for the potential energy in the Schrödinger equation yields anharmonic vibrational energies

$$E_\nu/(hc) = \beta\sqrt{\frac{D_e}{2\pi^2c^2\mu}}(\nu + \tfrac{1}{2}) - \frac{h\beta^2}{8c\pi^2\mu}(\nu + \tfrac{1}{2})^2, \tag{2.3}$$

where μ is the reduced mass of the molecule. The Morse potential is an excellent approximation of molecular potential energy for all diatomic molecules.

It only deviates significantly from the experimentally determined curve when the energy of the molecule is close to the dissociation limit [21].

Having worked out the energy eigenstates for the Morse potential, we can now express the physical quantities in Eq. 2.3 in terms of the well-documented molecular constants ω_e and $\omega_e x_e$ which appear in Eq. 2.1. To do this, I will assume that the terms beyond the first two are so small that they do not significantly contribute to the energy. Explicitly,

$$E_\nu/(hc) \approx \omega_e(\nu + \tfrac{1}{2}) - \omega_e x_e(\nu + \tfrac{1}{2})^2. \tag{2.4}$$

By equating Eq. 2.4 and Eq. 2.3, we can see that

$$\beta = \sqrt{\frac{2\pi^2 c^2 \mu}{D_e}}\omega_e \tag{2.5}$$

and

$$D_e/(hc) = \frac{{\omega_e}^2}{4\omega_e x_e}. \tag{2.6}$$

As I will describe in Section 2.2, the magnitude of the dissociation energy for a molecule directly affects the sensitivity that molecule exhibits to variation in the proton-to-electron mass ratio. Thus, the Morse potential approximation gives us a quick means of determining which molecules are promising for our QLS experiment, since ω_e and $\omega_e x_e$ are documented for a variety of molecules [22].

2.1.1 Molecular State Energy and Dependence on μ

The total potential energy of a molecule includes electronic and rotational energy terms in addition to the vibrational terms well-approximated by Eq. 2.4. The rotational energy comes from the molecule's angular momentum and can be expressed as

$$E_J = \frac{\hbar^2}{2I} J(J+1), \tag{2.7}$$

where I is the molecule's moment of inertia, J is its total angular momentum quantum number, and $B_e hc \equiv \hbar^2/(2I)$ is a rotational constant. Therefore, a molecule in a particular quantum state with electronic energy T_e has an energy

$$E/(hc) = T_e + \omega_e(\nu + \tfrac{1}{2}) - \omega_e x_e(\nu + \tfrac{1}{2})^2 + B_e J(J+1). \tag{2.8}$$

While this molecular state is not explicitly dependent on the proton-to-electron mass ratio μ, it has implicit dependence through multiple parameters in this equation. DeMille *et al.* [3] reveals this dependence through the following argument. First, assume that the mass of an electron m_e is fixed: Measuring variation in μ is now equivalent to measuring a change in the mass of a proton m_p. Fixing m_e results in no loss of generality and implies that dependence on μ is equivalent to dependence on m_p, which itself is proportional to the reduced mass of the two-atom system. Therefore, any dependence on the reduced mass in Eq. 2.8 corresponds to the same dependence on μ.

Recall that the frequency of oscillation ω of a harmonic oscillator is related to the oscillating mass M by $\omega \propto 1/\sqrt{M}$. This is likewise true for the harmonic term in Eq. 2.8: ω_e scales as $\mu^{-1/2}$. Furthermore, the constant

in the anharmonic vibrational term and the rotational constant B_e scale as μ^{-1} [3, 4]. Generally, T_e depends on the reduced mass of the nucleus and the electron. Since the nucleus is much heavier than the electron, the reduced mass is approximately equal to the mass of the electron. As a consequence, the dependence of T_e on nuclear mass and, therefore, on μ, is negligible.

2.2 Experimental Sensitivity

Variation in μ can be detected by precisely measuring the energy difference between two internal states with different dependences on μ. For levels $E'(\mu)$ and $E''(\mu)$, this difference is expressed as $\hbar\omega = E'(\mu) - E''(\mu)$. This corresponds to a relative change in μ of

$$\frac{\Delta\mu}{\mu} = \frac{1}{\mu}\left(\frac{\partial\omega}{\partial\mu}\right)^{-1}\Delta\omega = \left(\frac{\partial\omega}{\partial(\ln\mu)}\right)^{-1}\Delta\omega \tag{2.9}$$

where $\partial\omega/\partial(\ln\mu)$ is referred to as the absolute sensitivity of the transition [4]. The absolute sensitivity to variation in μ of a molecule in a particular state with an energy given by Eq. 2.8 is

$$\frac{\partial\omega}{\partial(\ln\mu)} = \frac{1}{hc}\frac{\partial E}{\partial(\ln\mu)} = -\frac{1}{2}\omega_e(\nu+\tfrac{1}{2}) + \omega_e x_e(\nu+\tfrac{1}{2})^2 - B_e J(J+1). \tag{2.10}$$

This demonstrates that a fractional change in μ can be detected by precise measurements of the energy of two different vibrational or rotational states. However, as noted in Ref. [4], transitions between states with large differences in J are not allowed by selection rules, and B_e is typically smaller than ω_e, so

transitions between vibrational states tend to be more sensitive.

Furthermore, the magnitude of the sensitivity grows approximately linearly at low vibrational states, but the term proportional to ν^2 rapidly reduces the sensitivity of vibrational levels close to the dissociation energy D_e. The absolute sensitivity is maximized at vibrational states with energies $E_\nu \approx .75D_e$, corresponding to a peak in sensitivity $\partial\omega/\partial(\ln\mu) \approx .25D_e$ [3, 23]. This peak sensitivity leads to the first important consideration in choosing a spectroscopy molecule for this experiment: Molecules with deeper molecular potentials will exhibit more sensitivity to variation in μ.

To make the most precise measurement of $\Delta\mu/\mu$, we need to use a transition that reduces the statistical uncertainty $\delta\omega$ with which we can measure $\Delta\omega$. The precision of our measurement is dependent on the linewidth of the transition Γ. Assuming white noise, it is given by

$$\delta\omega = \frac{\Gamma}{\sqrt{M}S/\delta S}, \tag{2.11}$$

where $S/\delta S$ is the signal-to-noise ratio and M is the number of independent measurements [4]. Performing an experiment on a transition with a narrow linewidth thereby maximizes the precision of the measurement. For instance, if we use a transition between the ground electronic state and an excited state which cannot decay into any other state as suggested in Ref. [3], it will have a narrow linewidth if it is forbidden by spin selection rules (which we can drive via spin-orbit coupling) [4]. Thus, we will look for states with differing spin multiplicities.

To enhance the sensitivity of the measurement, we will measure transitions between a state near the peak sensitivity to μ and a state with very little sensitivity to μ. However, driving a transition between two states with a large energy difference and the aforementioned criteria is difficult to accomplish [4], so we will focus on transitions between states of nearly degenerate energies.

2.3 Promising Molecules

We have now identified the most important considerations for the proposed measurement. A promising molecule should have a deep molecular potential (a large dissociation energy), with another electronic energy level of a different spin multiplicity dipping into the ground state (that is, the two levels have the same dissociation energy). Furthermore, its molecular constants ω_e and $\omega_e x_e$ should be relatively low. Eq. 2.4 indicates that if these constants are small, the vibrational levels should be closely-spaced, which increases the likelihood of an accidental degeneracy between a state of high absolute sensitivity to μ and a state with low sensitivity to μ. If the lower electronic level state is in a vibrational state corresponding to an energy of approximately $.75D_e$, we maximize its μ-dependence. A transition between this level and a higher electronic energy level that is nearly in its vibrational ground state maximizes the difference in μ-dependence between the levels.

Generally, we will confine our search for molecules with these properties to those that are homonuclear. In homonuclear molecules, symmetry eliminates half the rotational states and forbids electric dipole (E1) transitions within an

electronic state (transitions proceeding as electric quadrupole transitions will have narrower linewidths), as well as other systematic effects [4].

The oxygen isotope $^{16}O_2{}^+$ fulfills the above criteria, making it experimentally promising. We discuss the details of its useful transitions in Ref. [4], the most important aspects of which I outline below. With a ground state energy of 54 600 cm^{-1}, oxygen has a deep electronic potential. The absolute sensitivity of the vibrational states in the three lowest electronic levels of oxygen is shown in Fig. 2.1. The two lowest electronic states, $|X^2\Pi_g\rangle$ and $|a^4\Pi_u\rangle$ have different spin multiplicities (and the a state is coupled to the nearby $|A^2\Pi_u\rangle$ state with the same multiplicity as the ground state, so we should be able to drive the transition). Furthermore, we have identified multiple transitions with energy differences less than 10 cm^{-1}, shown in Fig. 2.2. Particularly promising is the transition between the $|X, \nu = 21\rangle$ state and the nearly degenerate $|a, \nu = 0\rangle$ state, which has an absolute sensitivity of $-\partial\omega/\partial(\ln\mu) = 12\ 600$ cm^{-1} (contributions from the third term in Eq. 2.10 should be on the order of 100 cm^{-1}). The linewidth of this transition falls within the range $\Gamma/(2\pi) = 0.07 - 10$ Hz. The high sensitivity combined with the narrow linewidth of this transition should yield a statistical precision of $\delta\mu/\mu$ on the order of 4×10^{-18} in 1 day.

I searched the literature to determine which other homonuclear diatomic molecules fulfill the criteria described above and, therefore, could also be used to make a high precision measurement of $\delta\mu/\mu$. I began by checking the homonuclear entries listed by Huber and Herzberg in Ref. [21]. This book compiles the results of past spectroscopy experiments and lists molecular constants for the known electronic energy levels of many diatomic molecules. Its

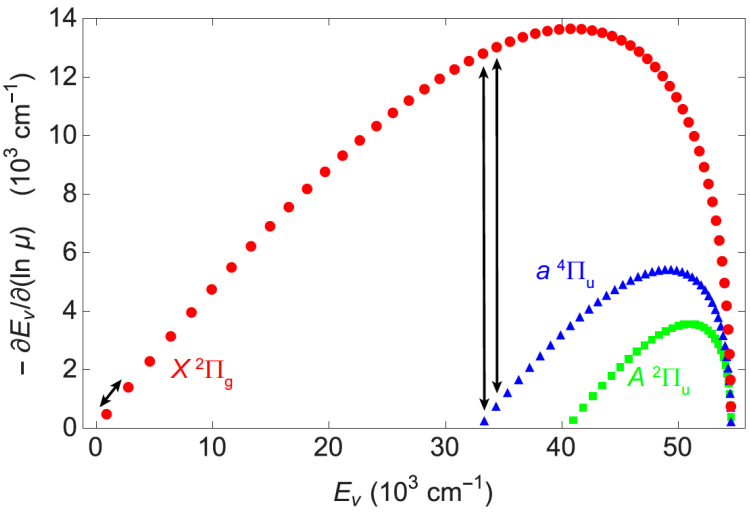

Figure 2.1: Absolute Sensitivity of Oxygen States to μ Variation. The sensitivity is calculated for the three lowest electronic energy levels using a Morse potential approximation. This figure is from Ref. [4], where we discuss the sensitivity of the three transitions marked by arrows.

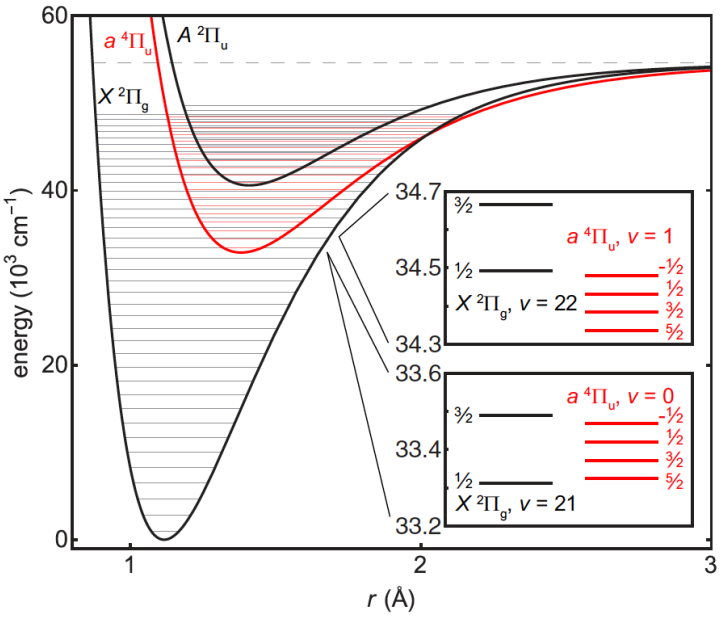

Figure 2.2: Morse Potential Curves for the Lowest Electronic Levels in $^{16}O_2{}^+$. Experimentally measured vibrational levels are shown as horizontal lines. The inset shows nearly degenerate energy levels that are suitable for high absolute sensitivity to variation in μ. This figure is from Ref. [4].

data on electronic ground states tends to be reliable, but it often lists imprecise or contested information regarding excited levels. After preliminarily identifying candidate molecules from this source, I performed a citation-based search to find articles that reference Huber and Herzberg and discuss homonuclear molecules. These other articles typically list more precise values of ω_e and $\omega_e x_e$, clarify the existence of excited states (with more precise potential depths listed for these states), and occasionally reveal other homonuclear diatomic molecules with similar properties. N_2, Cl_2, Br_2, and $I_2{}^+$ were among the most promising molecules this search revealed.[2] Based on the depths of these molecules' potential wells, their absolute sensitivities to variation in μ (Eq. 2.10) should all be within an order of magnitude of the absolute sensitivity of $^{16}O_2{}^+$. Their molecular properties are documented in Ref. [21, 24–26] and compiled in Appendix B alongside those of $^{16}O_2{}^+$ [4, 27, 28] for reference.

Unfortunately, my search was limited by the focus and precision of past spectroscopy experiments. The constant $\omega_e x_e$ in particular was only available for a small portion of homonuclear diatomic molecules. Frequently, their uncertainties are high or their values are disputed [21]. This is to say that my search is not exhaustive, and other molecules beyond those discussed here might be equally useful for making a precision measurement of μ variation.

Many of the molecules listed have a much higher density of vibrational states than oxygen, since their values of ω_e and $\omega_e x_e$ are smaller by about

[2] I did not limit this search based on which molecules our ion trap is capable of trapping, nor which would be easiest to manipulate with our $^9Be^+$ logic ion. This is primarily because spectroscopic information on cations is scarce, but also because I hope for this list of molecules to be useful for other lab setups as well as our own. The molecules listed here refer to their most common isotopes.

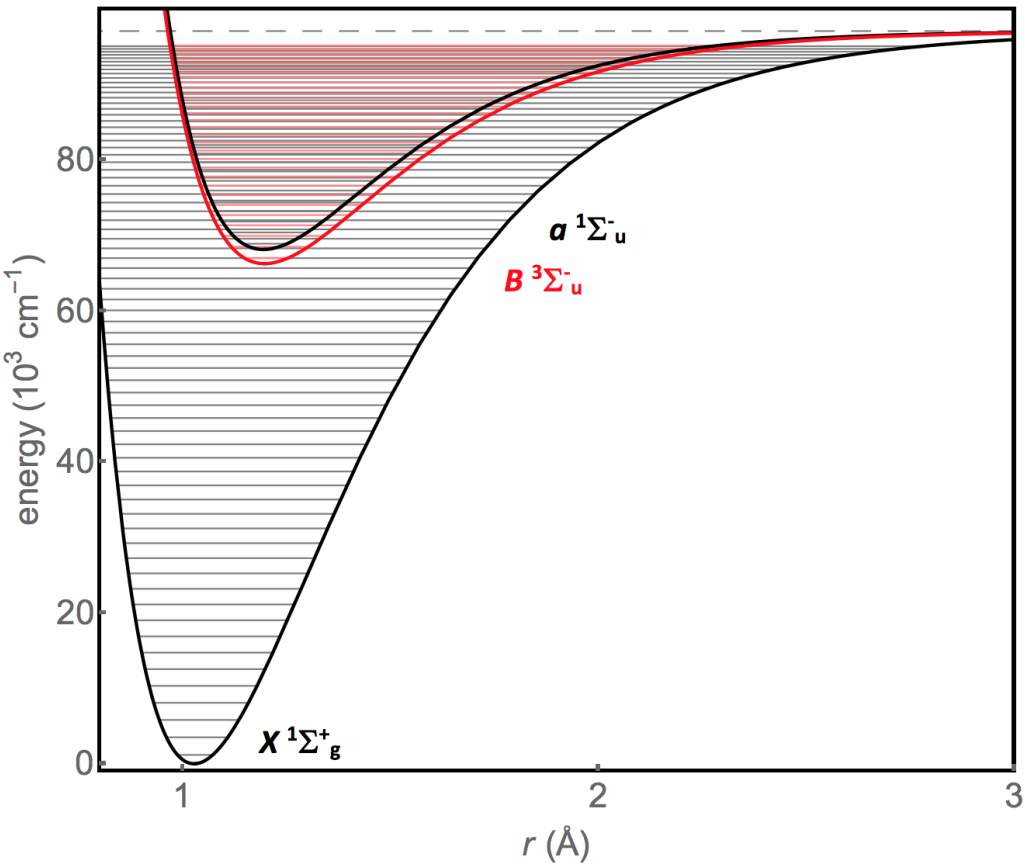

Figure 2.3: Morse Potential Curves for the Lowest Electronic Levels in $^{14}N_2$. Calculated vibrational energy levels are shown as horizontal lines. The near degeneracy of the $|X, \nu = 36\rangle$ and $|B, \nu = 0\rangle$ states, combined with a large dissociation energy, indicates that this transition is highly sensitive to changes in μ. The close a state could provide spin-orbit coupling to make this transition feasible.

an order of magnitude. N_2 is the exception, but is nevertheless a promising candidate due to its exceptionally deep ground state potential well.

Since the $|X^1\Sigma_g^+\rangle \leftrightarrow |B^3\Sigma_u^-\rangle$ transition in $^{14}N_2$ should have the highest absolute sensitivity to variation in μ among the transitions tabulated, I calculated this molecule's energy levels (Eq. 2.8). A Morse approximation and estimated values for these states' vibrational levels are shown in Fig. 2.3, alongside those of the $|a^1\Sigma_u^-\rangle$ state which, through spin-orbit coupling with the B state, could make this transition feasible. In particular, the $|X, \nu = 36\rangle$ state is nearly degenerate with the $|B, \nu = 0\rangle$ state, with an energy difference of only 23 cm^{-1}, indicating the high relative sensitivity of this transition. Furthermore, the $|X, \nu = 36\rangle$ state has an energy $E_{36} \approx .69D_e$, which, combined with the depth of nitrogen's ground state potential well, signifies that this transition should have an absolute sensitivity to μ larger than that of oxygen. Indeed, the absolute sensitivity of this transition is $-\partial\omega/\partial(\ln\mu) = 23\ 600$ cm^{-1}, about twice that of the proposed transition in $^{16}O_2{}^+$. A more detailed analysis of nitrogen is needed to determine the linewidth of this transition and, thus, the statistical precision $\delta\mu/\mu$ of our experiment.

The presence of such a transition in $^{14}N_2$ yields two important pieces of information. First, it indicates that the spacing of vibrational levels is sufficiently narrow to find nearly degenerate levels with energies approximately $.75D_e$ for molecules with somewhat large ω_e and $\omega_e x_e$; the magnitude of D_e, setting the limit of the absolute sensitivity, is a more important consideration than the density of vibrational levels. It also confirms that the particular arrangement of energy levels in $^{16}O_2{}^+$ that make it suitable for our QLS ex-

periment is not unique. Precision measurements of μ variation can be made with many different molecules.

Chapter 3

Ion Trap Parameterization and Resonances

To use beryllium as the logic ion in quantum logic spectroscopy experiments, we need to understand the dynamics we should expect this ion to exhibit. If we desire to prepare a specific state in oxygen, hope to carefully manipulate it, or simply confirm that it is successfully loaded and trapped alongside the beryllium, we need to understand how beryllium behaves in the ion trap. In particular, the Coulomb force will couple the motion of beryllium to oxygen. Thus, measuring the changes in resonances of beryllium will be the most direct means to identify trapped oxygen. In this chapter, I will begin by giving an overview of the theory behind the linear Paul trap we use to trap ions, which will lead to the equations governing the motion of trapped ions. We will use this framework later in this chapter to identify key pieces of information which constitute this quantum toolbox and will be useful for interpreting and

preparing the internal states of oxygen molecules.

3.1 Trap Properties

An ion trap is an apparatus designed to confine a charged particle to a well-defined region of space using electromagnetic fields. Our lab is interested in trapping positively-charged atoms and molecules, so our ion trap uses electric fields to confine ions. The process of trapping ions is complicated by Earnshaw's Theorem: A collection of point charges cannot be kept in a stable equilibrium only by electrostatic interactions [29]. To address this, such traps need to use dynamic electric fields created by oscillating potentials in addition to static fields created by static potentials. Our lab uses a linear Paul trap built by Shenglan Qiao to create the desired trapping field [30].

Originally designed by Wolfgang Paul [31], a linear Paul trap generates a three-dimensional trapping potential where the oscillating field generates a time-averaged force on trapped charges towards the center of the trap in the two radial dimensions and electrodes with static (DC) potentials are arranged axially to confine charges in the third dimension. To trap ions, these traps use an oscillating potential in the radio frequency (RF) range. Our trap has four rod-like electrodes extending in the z-axis to produce these potentials. The RF potential is applied to two non-adjacent electrodes, and the remaining two electrodes are segmented into five sections with DC voltages which increase in magnitude with distance from the center. Figure 3.1 illustrates the Paul trap constructed for our experiments. The corresponding segments on the

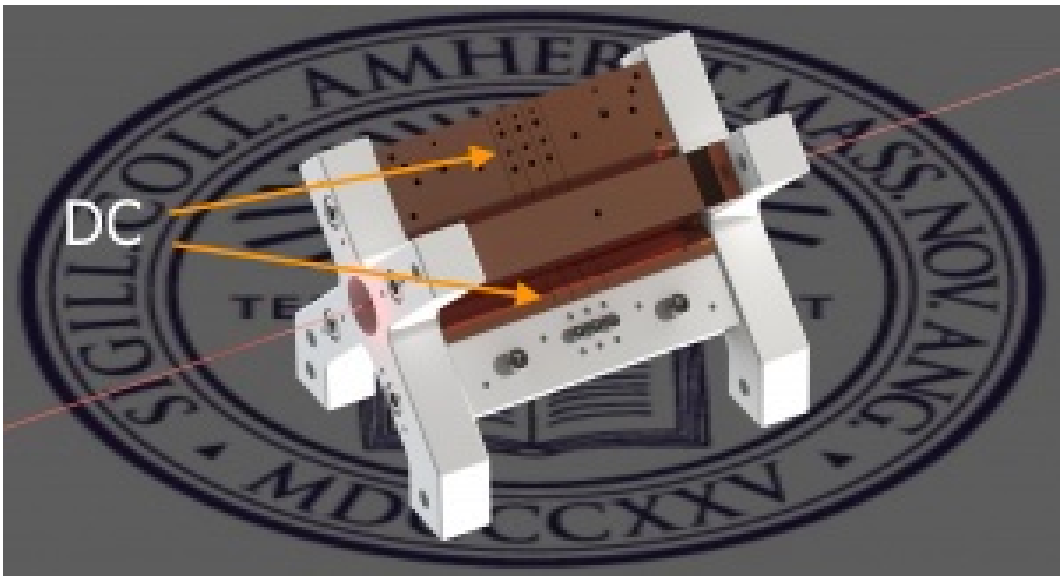

Figure 3.1: Solidworks Rendering of the Hanneke Lab Paul Trap. The four electrodes are arranged around the axial dimension of the trap. The two segmented electrodes with applied DC voltages are indicated by the orange arrows; the other two are the unsegmented RF electrodes. This rendering was created by Jim Kubasek.

two electrodes are typically set to the same voltage, but we can adjust this differential to shift the equilibrium position of the trapped ions if desired. When they are set to the same voltage, I will refer to the voltages on these electrodes as $\boldsymbol{V} = (V_1, V_2, V_3, V_4, V_5)$.

As discussed in Section 1.3.1, the trapping potential of such a trap is quadratic and saddle-shaped (Fig. 1.1). The idealized and most general form of the quadratic trapping potential Φ generated by these traps can be written

$$\Phi = \Phi_0(Ax^2 + By^2 + Cz^2), \tag{3.1}$$

where A, B, and C have units of inverse length squared and Φ_0 is some time-

dependent electric potential. For an arbitrary voltage on each electrode, one could create a numerical model that describes the behavior of these parameters. Instead, we parameterize Φ with relevant length scales and electric potentials and measure dimensionless parameters A, B, and C. Furthermore, we treat the potentials created by the RF and DC electrodes separately, with the acknowledgement that the total potential experienced by an ion in the trap is a superposition of these two potentials.

The potential created by the DC electrodes Φ_{DC} is often parameterized in terms of the potential applied to the DC electrodes U_0 and a characteristic trap length factor z_0, which is conventionally taken to be half the length of the center electrode. That is,

$$\Phi_{\mathrm{DC}} = \frac{U_0}{{z_0}^2}(Ax^2 + By^2 + Cz^2). \tag{3.2}$$

Our trap uses five pairs of DC voltages applied to the electrodes to trap particles axially, so there is ambiguity in what U_0 is in this setup. Generally, if the ions are confined to the center of the trap, they will experience a potential largely created by the trapping potential on the inner three pairs of electrodes. Thus, to a good approximation, we can treat the difference in voltage between the center pair and the adjacent pairs as U_0. I will discuss the minor effect of this treatment in the context of trap parameterization in Section 3.4.

Both the DC and RF potentials must satisfy Laplace's equation ($\nabla^2\Phi = 0$), so $A+B+C = 0$. Much work on ion trapping is done in the case of a trap with rotational symmetry about the z-axis, yielding $A = B = -C/2$ and, thus, a

quadrupolar potential. This rotational symmetry can be achieved by applying an identical array of DC voltages to each of the four electrodes surrounding the trap axis.

Our trap does not have this radial symmetry, since the two RF electrodes are set to DC ground. To ensure the potential equation always satisfies Laplace's equation, we introduce a constraining parameter σ and set $C = 1$. These changes give

$$\Phi_{\mathrm{DC}} = \frac{U_0}{{z_0}^2}\left[z^2 - \left(\sigma x^2 + (1-\sigma)y^2\right)\right]. \tag{3.3}$$

Notice that the symmetric trap is given by the condition $\sigma = 1/2$.

Unlike the quadrupole trap, our trap has well-defined x- and y-axes due to the constraint imposed by the system's Laplacian. This will become particularly important in the context of radial frequencies of oscillations (discussed in Sect. 3.2.2), as it breaks the degeneracy of the radial modes.

The potential generated by the RF electrodes is much easier to analyze. With an RF signal $V(t) = V_0\cos(\Omega t)$, the potential generated from the RF electrodes in the case of the ideal linear Paul trap is

$$\Phi_{\mathrm{RF}} = \frac{V_0}{2}\left(1 + \frac{x^2 - y^2}{{r_0}^2}\right)\cos(\Omega t), \tag{3.4}$$

where r_0 is the distance from the electrodes to the trap axis [32]. For our trap, $r_0 = 1.183$ mm. Charged particles will experience a net potential that is a sum of the RF and DC potentials.

3.2 Dynamics of One Trapped Ion

To easily understand the dynamics of a trapped ion, we need to determine the effective potential a charged particle will experience in the presence of the potentials given by Eq. 3.3 and Eq. 3.4. To do this, we introduce a correction factor designed to account for the fact that our linear Paul trap is not ideal. We subsequently recast the potentials experienced by a trapped particle as pseudopotentials where necessary. A pseudopotential is an approximation of a time-varying potential as a time-independent (averaged) potential. Following this approximation, we can break up the potentials experienced by a trapped ion into two parts: a static potential (the pseudopotential) and the time-varying potential which causes small-scale dynamics called micromotion. The purpose of this approximation is to easily identify the resonant frequencies of the ion's motion in the trap.

3.2.1 Axial Motion in a Non-Ideal Trap

Since the DC potential is already time-independent, we do not need to approximate it. Indeed, for the case of a single trapped ion, we can read the axial trap resonance directly from Eq. 3.3 since this is in the form of a harmonic oscillator, and the RF potential (Eq. 3.4) has no z-dependence. However, Eq. 3.3 does not accurately describe our trap. Unlike the ideal linear Paul trap, our trap is not perfectly symmetric. Additionally, there may be capacitances between the electrodes which alter the potential. We need to make an adjustment to account for these conditions in the form of a geometric constant

factor κ which attenuates the potential experienced by a particle. That is, $0 < \kappa < 1$ and a particle of mass m and charge q experiences an axial electric potential near the center of the trap of

$$\Phi_{\mathrm{z}} = \frac{\kappa U_0}{{z_0}^2}\left[z^2 - \left(\sigma x^2 + (1-\sigma)y^2\right)\right] = \frac{m}{2q}{\omega_z}^2\left[z^2 - \left(\sigma x^2 + (1-\sigma)y^2\right)\right], \quad (3.5)$$

where ω_z is the angular frequency of oscillations in the axial direction and can be expressed in terms of trap parameters and the trapped particle's charge-to-mass ratio:

$$\omega_z = \sqrt{\frac{2\kappa q U_0}{m{z_0}^2}}. \quad (3.6)$$

I will discuss the theory behind κ in more detail in Section 3.4. For the moment, it suffices to state the axial potential and angular frequency of oscillations.

3.2.2 The Pseudopotential Approximation of Radial Motion

Unlike the DC potential, the RF potential needs to be approximated as a pseudopotential due to the time-dependence of Eq. 3.4. To make this approximation, we assume that the frequency of oscillation Ω of the RF signal is sufficiently high to confine ion motion near the trap axis. Drewsen and Brøner discuss this condition in Ref. [33]. The result is that Eq. 3.4 can be approximated by the pseudopotential

$$\Phi_{\mathrm{r}} = \frac{m}{2q}{\omega_{\mathrm{r}}}^2(x^2 + y^2) \quad (3.7)$$

for a particle of mass m and charge q in the trap. In the above equation, written in the form of a harmonic oscillator, ω_{r} is the radial angular frequency of oscillations experienced by an ion in the trap due to the RF potential, related to the other trapping parameters by

$$\omega_{\mathrm{r}} = \frac{qV_0}{\sqrt{2}m\Omega {r_0}^2}. \tag{3.8}$$

Since both Φ_{DC} and Φ_{r} contain a radial component, Eq. 3.8 does not fully describe the radial motion of the trapped particle. By the principle of superposition, the radial pseudopotential experienced by a trapped particle is altered by the presence of the DC electrodes: It is enhanced in the axis along which the DC electrodes are situated (the x-axis) and reduced in the radial axis orthogonal to them (the y-axis). Additionally, Φ_{DC} also splits the radial frequency of oscillations into two distinct frequencies, one corresponding to motion along the x-axis and the other to motion along the y-axis. The total radial potentials of such a system can be written

$$\Phi_x = \frac{m}{2q}\left(\omega_{\mathrm{r}}^2 - \sigma {\omega_z}^2\right)x^2 \tag{3.9}$$

and

$$\Phi_y = \frac{m}{2q}\left(\omega_{\mathrm{r}}^2 - (1-\sigma){\omega_z}^2\right)y^2, \tag{3.10}$$

which correspond to angular frequencies of oscillations

$$\omega_x = \sqrt{{\omega_{\mathrm{r}}}^2 - \sigma {\omega_z}^2} \tag{3.11}$$

and

$$\omega_y = \sqrt{{\omega_\mathrm{r}}^2 - (1-\sigma){\omega_z}^2}. \tag{3.12}$$

Since the linear Paul trap generates a potential that is well approximated as harmonic, while one ion is confined to the linear Paul trap, Eq. 3.6, Eq. 3.11, and Eq. 3.12 characterize the motion of the ion. To predict the motion of trapped ions, we first must determine our trap's values of κ and σ. The remainder of this chapter is dedicated to constructing and analyzing experiments meant to determine these values.

3.3 Experimental Design

Having established the theoretical framework governing the motion of a single trapped ion in both the axial and radial dimensions, I will walk through the experiment I performed to discover the frequency of oscillations exhibited by a trapped ion using detections of resonances. This section describes the experimental setup used to discover the ion's motion in the trap, the results of which will be discussed throughout the remainder of the chapter.

A trapped ion will move at the real frequencies corresponding to the angular frequencies of oscillations given by Eq. 3.6, Eq. 3.11, and Eq. 3.12. Such an ion can be driven to move with very large amplitudes if we apply a drive at a frequency f corresponding to one of these angular frequencies ($f = \omega/(2\pi)$) to the ion's potential well. To do this, we add a low-voltage sine wave signal to the fourth DC electrode of the Paul trap. The peak-to-peak voltage of this signal should be lower than the trapping voltage on this electrode in order to

keep the ions in the trap. This modulates the trap potential minutely, causing the ion to move. As the signal's frequency approaches a resonant frequency, the ions will oscillate at large amplitudes. This reduces the photon emission from the ions primarily because the motion induces a doppler shift in the ion resonance, stopping the laser from driving electronic transitions.

When we first set up this experiment, we observed the ions by detecting photons emitted by the ions in the path of the detuned laser beam with a camera. We used a function generator to produce the oscillatory signal on the fourth electrode and drive the ions. In this case, the resonances were detected by the ion blurring and, at resonance, disappearing as its photon emission rate sharply decreased, as shown in Fig. 3.2. We observed the desired behavior using this method, and the resonances were seen in the range of 100 kHz − 800 kHz; however, this method was slow, imprecise, and difficult to analyze statistically. For instance, it was difficult to determine the relative depths of these resonances, which indicates how easy they are to drive (and, due to the asymmetry of our trap, indicates which resonance corresponds to which axis).

We solved these issues by automating the process. Instead of viewing the ions on a camera, we directed the scattered light to a photomultiplier tube (PMT) to use a photon count as a quantitative measure of the ion's visibility. This change substantially improves the rate at which we can collect data, since, to detect the ions, the camera requires an exposure time on the order of 100 ms and the PMT requires an exposure time on the order of 1 μs. Instead of tuning the driving frequency by hand, we use a Direct Digital Synthesizer

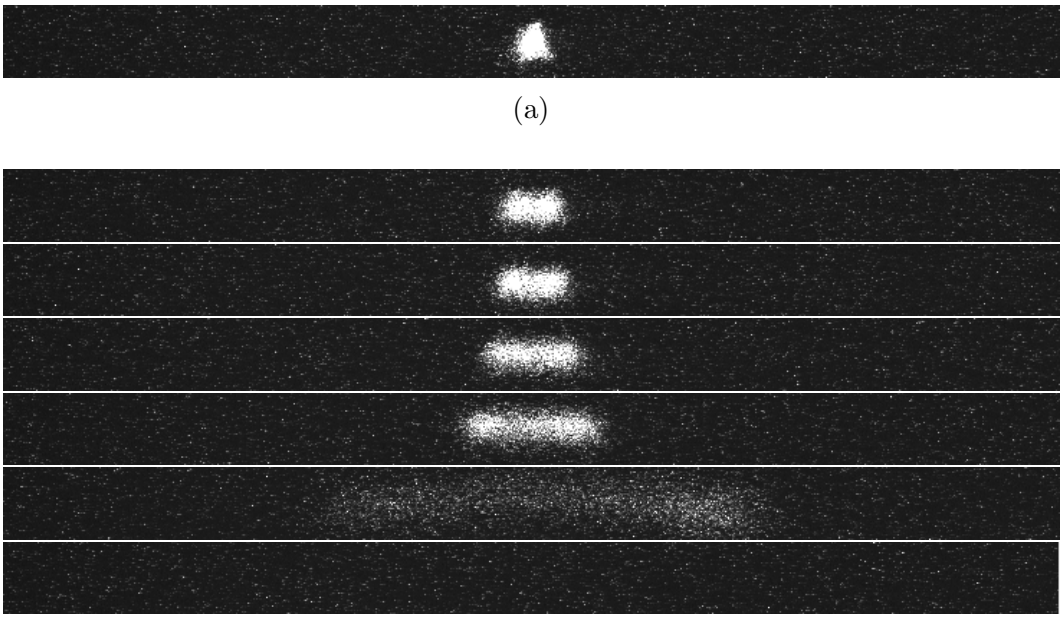

(a)

(b)

Figure 3.2: Photograph of a Beryllium Ion in a Modulating Trap Potential. (a) A single trapped beryllium ion with the trap potential modulation turned off and trapping voltages corresponding to $U_0 = 3$ V. (b) The same ion in the presence of a driving signal. From top to bottom, the modulation frequency is increased in 10 kHz steps, from 280 kHz to 330 kHz. Notice the elongation of the ion as the modulation frequency approaches the resonant frequency (329 kHz). For scale, the crystallized ion in (a) is approximately 10 μm wide.

board (DDS), Analog Devices model AD9910, to output an analog signal given a digital one. The main advantage of this approach is that we can design a program to send the signal and collect our data automatically, essentially using the DDS board as a programmable function generator.

The DDS has a signal output limited by attenuating circuit elements following it (namely, a transformer and a variable attenuator). These elements prevent the system from outputting substantial signals of frequencies lower than 10 MHz. I initially used a frequency mixer in combination with a low-

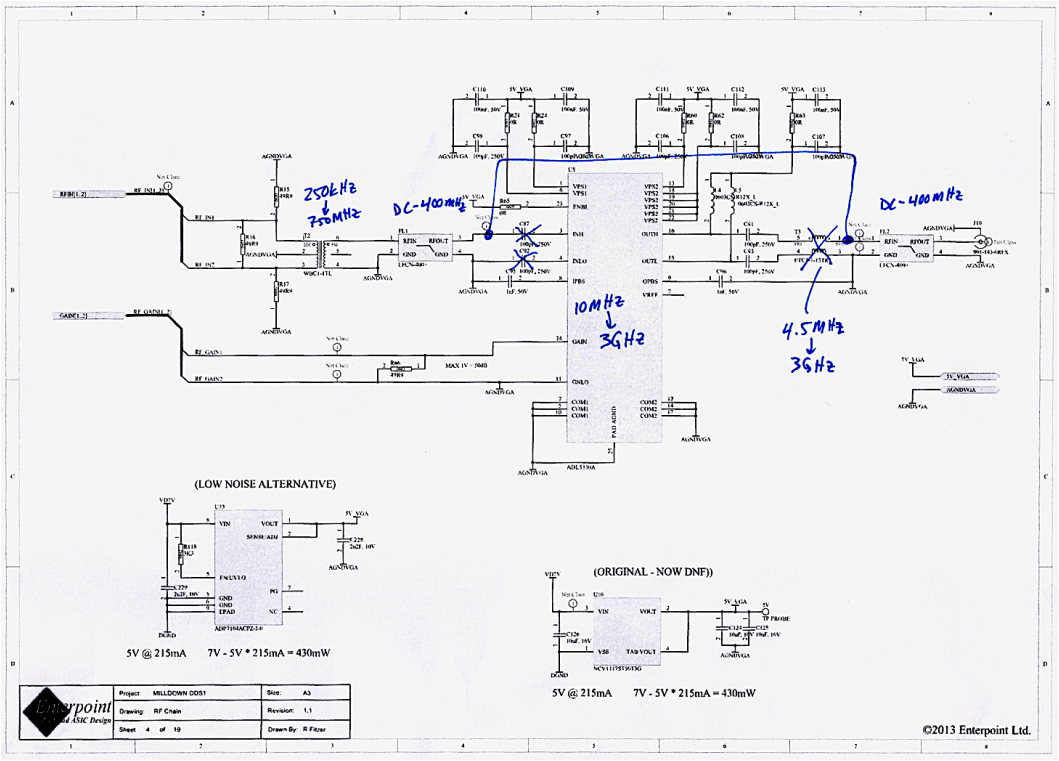

Figure 3.3: Hacked DDS Board Circuit Diagram. The markings show the changes made to the DDS board to bypass its frequency limitations.

pass filter to overcome this limitation, but the resulting signal was not a perfect sine wave. After checking the results of investigations with this setup against our earlier setup, we determined that this signal was likely driving harmonics of the trap resonances. To get unambiguous data, we scrapped this setup entirely and instead bypass the bandwidth-limiting components in the DDS board directly. Brian Crepeau made the adjustments to the DDS board to produce the desired output. These are shown in Fig. 3.3.

I used our lab's Quantum Logic Ion Control (QLIC) program to read and execute a script containing our experimental procedure. The front-end of

QLIC is in LabView, and its experiments are written in python scripts. It can identify variables to scan and record average photon counts from the PMT at each step of the scan. It can be used to send pulses to the AOMs, allowing us to control which beam (resonant, detuned, or repump; see Sect. 1.3.3) enters the ion trap at a given time. This particular experiment uses a pulse of the detuned beam to cool the ions from room temperature, then switches to a brief pulse of the resonant beam for Doppler cooling. Next, we trigger the DDS which sends the driving signal to the ions. We collect the data immediately after the pulse ends, while the resonant beam is on the ions. The data we collect at a given frequency is averaged for analysis and recorded as a histogram.

In our typical operating sequence, QLIC scanned frequencies of 100 kHz to 800 kHz in increments of 1 kHz steps, each of which was run for 100 experiments with detection windows of 0.5 ms each, which is large enough to yield average counts of tens of photons. Our default driving amplitude was between 400 $\mathrm{mV_{pp}}$ and 600 $\mathrm{mV_{pp}}$ at the source (it passes through a 10 kHz RC low-pass filter en route to the electrode). The modulation amplitude has some minor frequency-dependence, which is shown in Appendix C. These amplitudes were necessary for driving the radial modes, but such scans often sacrificed precision on the axial mode frequencies. In these cases, we typically repeated the scan with a finer step size and a lower driving frequency to achieve better resolution. In particular, we occasionally brought the driving amplitude to approximately 200 $\mathrm{mV_{pp}}$ to pinpoint the location of the axial resonant frequency. Once we found a resonance, we typically scanned over a small range (< 100 kHz) at a $100 - 500$ Hz step size to clearly display the resonance.

3.4 The Geometric Constant

Over the past few years, our lab has refined its techniques for measuring κ, the trapping parameter dependent on trap geometry which attenuates the axial potential and was introduced in Sect. 3.2.1. Shenglan Qiao discusses the theory behind κ in her thesis, but did not complete the discussion due to ambiguity in the literature [30]. Last year, Edward Kleiner began our lab's measurements of κ. He measured the ions' relative positions from photographs, and made two different measurements of κ: 0.1345 and 0.1136 [8]. Unfortunately, it is not clear whether these measurements were in statistical agreement, and the method of measurement was imprecise. I hope to unify these past investigations by making a more statistically rigorous measurement of κ.

I determine the value of κ for our trap by measuring the observed resonant frequencies of a single trapped ion at different axial trapping voltages, then fitting the data to Eq. 3.6. In order to accomplish this, I change the voltages $\boldsymbol{V} = (V_1, V_2, V_3, V_4, V_5)$ to alter the shape of the potential well. We kept $V_3 = 0$ V and took two sets of data. First, we set $V_1 = V_5 = 10$ V and found the resonances for various $V_2 = V_4 = V$. In the next set, we found resonances for various $V_1 = V_2 = V_4 = V_5 = V$. We can relate this to the parameter U_0 in Eq. 3.6 with the identity $U_0 = V$ in the latter case, but since our trap contains five DC electrodes as opposed to the three considered in the derivation of Eq. 3.6 by Raizen et al. in Ref. [32], it would be inaccurate to claim the same identity in the former case. As such, we will do our analysis on the case where we alter all voltages on the non-central electrode segments identically. The case where the end segments are set to 10 V will give us an indication of the

inaccuracy of the aforementioned identity.

This data, taken early in my year-long investigation, was collected by the first method outlined in Sect. 3.3. Specifically, I observed the resonances as maximally blurred ions on an image of the center of the trap captured by a camera, and the driving frequency was sent to the electrode by a function generator outputting a sine wave. Later, I collected this data using the PMT method, and determined that these measurements were accurate (corresponding data points are within uncertainty of each other). The result of this investigation is shown in Fig. 3.4.

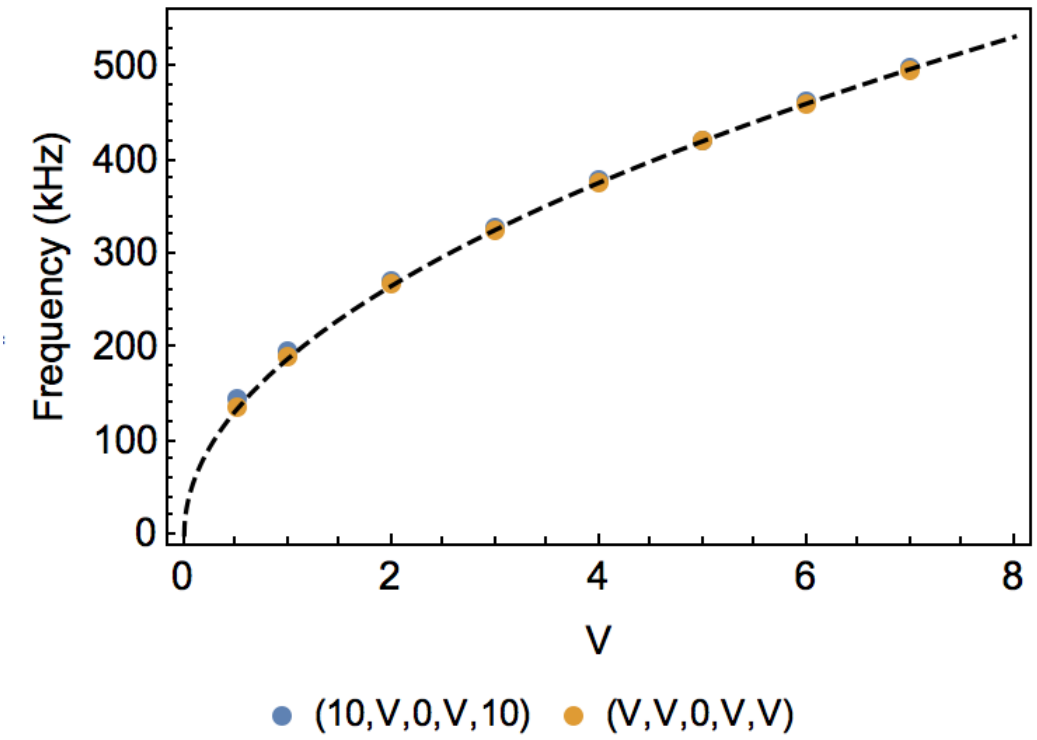

Figure 3.4: Potential Well Scaling of the Axial Resonance. The dashed line represents a square root fit of the orange data points. From this fit, we determine $\kappa = 0.147 \pm 0.002$.

While we analyzed the set of data for which we varied all four outer electrode voltages identically, this graph clearly shows that there is little difference between this and the case in which $V_1 = V_5 = 10$ V, especially at higher trapping voltages. At lower trapping voltages, the axial resonant frequency was slightly higher when the outer electrodes were set to 10 V. Our fitting equation yielded $2\kappa e/(2\pi)^2 m {z_0}^2 = 3.54(6) \times 10^{10}$ kg^{-1}m^{-2}C, with the uncertainty determined by the standard error in the fitting parameter. The characteristic trap length z_0 is typically taken to be half the length of the central electrode, which is 1.50 mm in our case. With this, we find $\kappa = 0.147 \pm 0.002$.

This value is higher than those measured by Kleiner, but with the precision on his measurements unknown, it is unclear whether this is statistically different. Regardless, our measurement is based on a best fit curve of many data samples and is, therefore, more statistically rigorous. Also, due to myriad improvements made to the laser system over the past year, my determination of κ was not impeded by many of the issues that Kleiner faced.

3.5 The Radial Asymmetric Ratio

To complete our parameterization of Qiao's Paul trap, we still need to determine the radial asymmetric ratio σ for our trap. We accomplish this by observing the locations of the three resonances of a single trapped $^9Be^+$ ion in the trap. This ratio can determined by rearranging Eq. 3.11 and Eq. 3.12 to

solve for ${\omega_r}^2$. Setting these equations equal to each other, we get

$$\sigma = \frac{1}{2}\left(\frac{{\omega_y}^2 - {\omega_x}^2}{{\omega_z}^2} + 1\right). \tag{3.13}$$

Likewise, by rearranging these equations to solve for σ, we can determine ω_r:

$${\omega_r}^2 = \frac{1}{2}\left({\omega_x}^2 + {\omega_y}^2 + {\omega_z}^2\right). \tag{3.14}$$

While keeping the RF frequency fixed at $\Omega/(2\pi) = 34.99$ MHz, we observed the resonances at axial trapping potentials ranging from $U_0 = 2$ V to $U_0 = 6$ V with a step size of 1 V. A typical scan made to find the radial modes (taken at $U_0 = 4$ V) is shown in Fig. 3.5.

As this figure indicates, motion along the y-axis is consistently more difficult to drive than motion along the x-axis for our trap. This is because our potential modulation occurs on a DC electrode, which is along the x-axis, angled 45 degrees relative to the z-axis, and perpendicular to the y-axis. Thus, x- and z-axis modes can be driven with lower amplitude signals than the y-axis mode. Occasionally, we needed to drive at a higher DDS amplitude to clearly distinguish ω_y from the noise inherent in counting photons.

The resulting σ values retrieved from scans at each U_0 are shown in Fig. 3.6. Although we assumed that σ is a constant, it clearly exhibits axial voltage dependence.[1] This does not affect any of our previous calculations, and a potential parameterized with a voltage-dependent asymmetric ratio $\sigma(U_0)$ still

[1] If we do decide to treat σ as a constant, this data yields $\sigma = 0.84(19)$. Clearly, this is not an accurate interpretation of the data shown in Fig. 3.6, but it gives us a quick and easy way of predicting the approximate locations of $^9Be^+$ radial resonances.

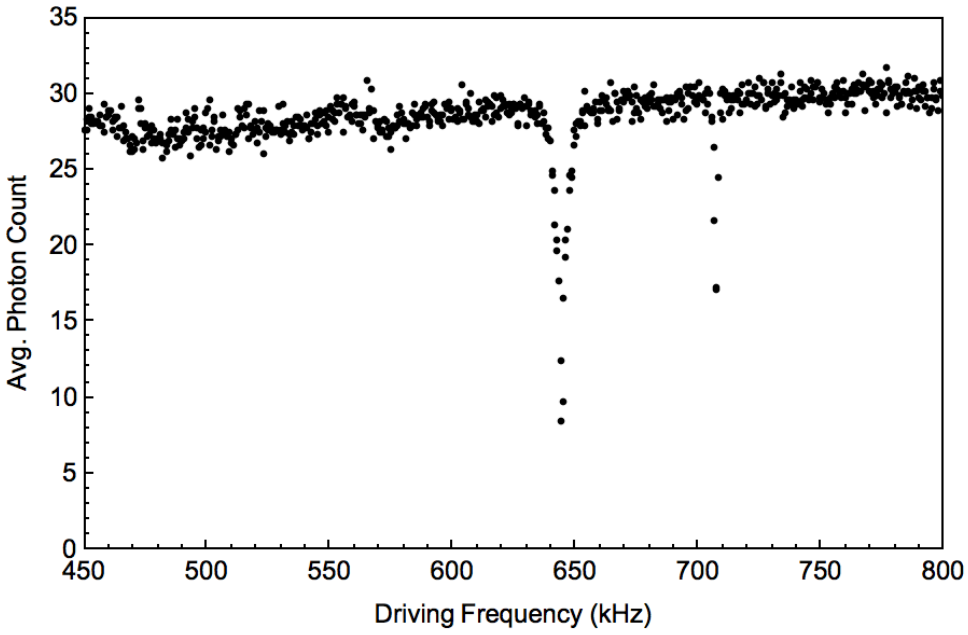

Figure 3.5: Trap Modulation Scan at $U_0 = 4$ V. Data was taken in steps of 500 Hz. This image is indicative of the typical data retrieved by a scan over driving frequencies. Radial modes are identified at $\omega_x/(2\pi) = 644$ kHz and $\omega_y/(2\pi) = 707$ kHz. The axial resonance is not shown; since it is very easy to drive, we searched for it separately with a lower driving amplitude.

satisfies Laplace's equation. However, a parameter that depends on an operating value such as U_0 does not have the same predictive power as a constant parameter.

Given the unexpected behavior of the radial asymmetric ratio, one might question the validity of our experiments. For instance, perhaps we misidentified some of the resonances. Fortunately, we can test whether these resonances were correctly identified by checking the value of ω_r retrieved for each set of resonances by using Eq. 3.14. Since we operated at the same RF amplitude and frequency throughout these experiments, ω_r should be constant. Indeed, we see

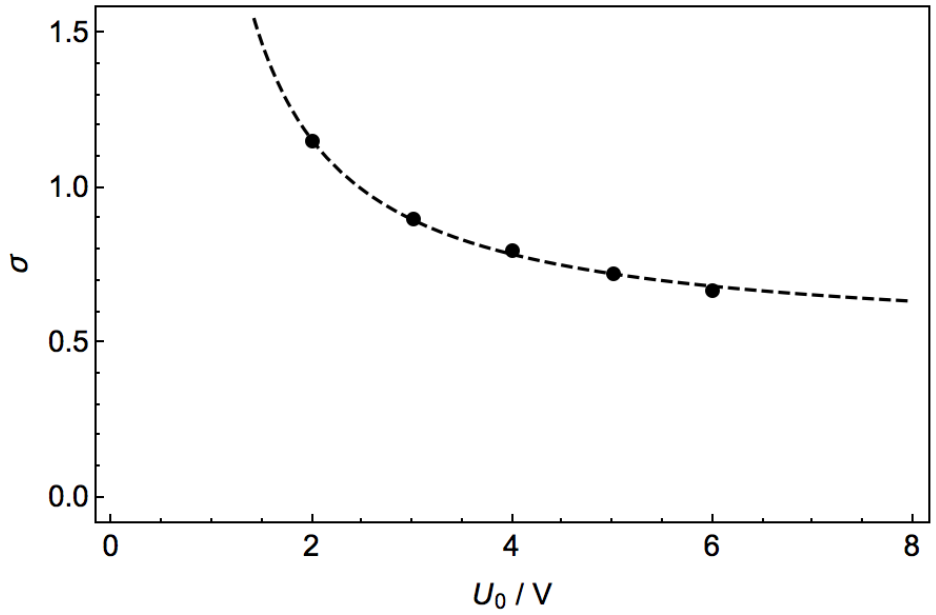

Figure 3.6: Experimentally Determined Values of σ. As the axial trapping voltage increases, our trap gets increasingly symmetric, given by the case where $\sigma = 0.5$. The dashed line is a fitting equation of the form $\sigma = [A/(U_0+B)]+0.5$, where $A = 1.01$ V and $B = -0.448$ V were determined from the fit.

only a narrow range of values for ω_r, with variations independent of axial trapping voltages. Taking the mean of these values, we find $\omega_r/(2\pi) = 725(2)$ kHz. The small standard deviation of this value gives us confidence in our findings.

No radial parameter is explicitly mentioned in the literature on Paul traps [6, 31, 32, 34]. Instead, these articles describe how closely the traps they use adhere to the case of the radially symmetric trap. The voltage dependence of σ could explain its absence.

While $\sigma(U_0)$ is not very useful as a trap parameter, it can still yield interesting information about our Paul trap based on its voltage dependence. I modeled the behavior of the parameter with the fitting equation $\sigma(U_0) =$

$[A/(U_0 + B)] + 0.5$, shown by the dashed line in Fig. 3.6 (with the fitting parameters $A = 1.01$ V and $B = -0.448$ V). This may not be the best fitting equation for the data, but it highlights one interesting trend: As the axial trapping voltage increases, $\sigma(U_0)$ approaches 0.5, which is the condition for a symmetric trap. In other words, the radial potential experienced by the ion gets increasingly symmetric in a stronger trap.

One explanation for this behavior could be the buildup of unequal charge (voltage) on opposite DC electrodes. At low trapping voltages, such an inequality could constitute a large fraction of the trapping voltage, which would push a trapped ion away from the radial center of the trap and toward one of the DC electrodes. At higher voltages, this difference would be fractionally smaller, so a trapped ion would reach a radial equilibrium closer to the trap's center. Viewing the scattered light from trapped ions on a camera, we have observed some voltage-dependence of the ions' position. Our camera is positioned directly between one set of DC and RF electrodes (at a 45 degree angle to the x- and y-axes). When we make large changes to the axial trapping voltages U_0 (more than 2 or 3 Volts), we typically need to readjust the camera's focus to center our image on the trapped ions again. However, this is just a cursory and anecdotal explanation for the observed behavior of $\sigma(U_0)$. Further investigation is needed to directly determine the cause of this behavior.

Having described $\sigma(U_0)$, we have concluded the parameterization of the Paul trap used in our experiments. Table 3.1 summarizes the results of these investigations. It displays the parameters used to describe the trapping potentials generated by the electrodes and lists typical operating values for other

Parameter	Value	Description
κ	0.147 ± 0.002	geometric constant
$\sigma(U_0)$	$\frac{1.01\text{V}}{U_0 - 0.448\text{V}} + 0.5$	radial asymmetric ratio
r_0	1.183 mm	distance from trap axis to electrodes
z_0	1.5 mm	characteristic trap length
U_0*	3.0 V − 10.0 V	operating DC potential
V_0*	185 V	operating RF amplitude

Table 3.1: Summary of Trap Parameters and Typical Operating Values. This table includes all of the important input parameters and values used to describe our trap. The parameters marked by asterisks are not set by the particular setup of our ion trap, and can be directly adjusted. For these parameters, the values given are typical operating values.

important and easily adjustable variables. With this information, we are equipped for spectroscopic experiments on multiple trapped ions.

3.6 Axial Dynamics with N Trapped Ions

Up to this point, we have considered the dynamics of a system composed of one trapped ion in our Paul trap in order to investigate the parameters appearing in the trapping potentials. Obviously, this is insufficient preparation for understanding how two ions behave when trapped together, the most basic condition for performing QLS experiments. Now I will shift my attention to the case in which multiple ions are co-trapped. When multiple ions are

trapped in a typical trapping potential, they spread out as a chain in the axial dimension. This is the dimension which is easiest to probe as well as that which contains the most useful information, so I will restrict this discussion to the axial motion of the ions, assuming that the ions' radial motion is small in comparison to their axial motion.

The ions in our trap are subject to two axial forces. First, they experience a trapping potential with a shape determined by the DC voltages of the Paul trap electrodes. Trapped at a sufficient distance from the electrodes, this potential is well approximated as harmonic in the center of the trap, where the trapped ions are located (ion motion tends to be on the scale of μm while the length from the ions to the edge of the center electrode is 1.5 mm). This is identical to the potential experienced by a single trapped ion. Second, each ion is repelled by the other ions in the trap via the Coulomb force. Thus, the total potential energy of the system with N trapped ions is

$$U = \sum_{i=1}^{N} \frac{1}{2} u_0 z_i^2 + \sum_{\substack{j,i=1 \\ j \neq i}}^{N} \frac{e^2}{4\pi\epsilon_0 \left| z_i - z_j \right|}, \tag{3.15}$$

where u_0 is a trapping constant, z_i (z_j) is the axial position of the i^{th} (j^{th}) ion in the trap, e is the charge of an electron (the total charge of one ion), and ϵ_0 is the permittivity of free space. Similarly, the kinetic energy of the system (in the Newtonian limit) can be written

$$T = \sum_{i=1}^{N} \frac{1}{2} m_i \dot{z_i}^2, \tag{3.16}$$

in which m_i is the mass of the i^{th} ion in the trap. It is important to keep in mind that Eq. 3.15 and Eq. 3.16 only describe the axial energies of the system.

We will use the general procedure followed by [34, 35], casting the energies in terms of q_i, the displacement of the i^{th} ion from its equilibrium position: We will define the set of values q_i as the solutions to the equations $\frac{\partial}{\partial z_i}\Big|_{z_i^0} = 0$, where z_i^0 is the classical equilibrium position of the i^{th} ion, which in turn allows us to define the mass-weighted coordinates $q_i{}' = \sqrt{m_i} q_i$. Using these coordinates, we can express the kinetic energy in a form that is independent of mass. Since the ions are confined to small oscillations on the scale of the trap, we can use a Taylor series expansion about the equilibrium positions z_i^0 to approximate our energy equations (Eq. 3.15 and Eq. 3.16). Neglecting terms of higher order than the leading (second-order) term, the potential is

$$\begin{aligned} U &= \frac{1}{2} \sum_{i,j} K_{ij} q_i{}' q_j{}', \\ K_{ij} &= \frac{1}{\sqrt{m_i m_j}} \frac{\partial^2 U}{\partial q_i \partial q_j}\Big|_{z_i^0}, \end{aligned} \tag{3.17}$$

and the Lagrangian of the system can thus be written:

$$L = \frac{1}{2} \sum_i \dot{q_i}'^2 - \frac{1}{2} \sum_{i,j} K_{ij} q_i{}' q_j{}'. \tag{3.18}$$

We use the Lagrangian to retrieve the axial equations of motion for this system, which yield a linear system of equations with the solution $q_i{}' = q_i^{0\prime} e^{i\omega t}$. This system of equations can be diagonalized to give the normal modes of the

ions in the trap: The normal modes α are given by

$$\sum_j K_{ij}\beta_j^{\alpha\prime} = \lambda_\alpha \beta_i^{\alpha\prime}, \tag{3.19}$$

where λ_α is the eigenvalue corresponding to the eigenvector β^α. Since K_{ij} is a hermitian matrix, these eigenvalues are all real, and are related to the frequency of the normal mode oscillations Ω_α by the relation $\lambda_\alpha = {\Omega_\alpha}^2$ when $\lambda_\alpha > 0$ for any α. Additionally, the normal mode coordinate ${q_\alpha}'$ corresponding to the normal mode α is

$${q_\alpha}' = \sum_i \beta_i^{\alpha\prime} {q_i}'. \tag{3.20}$$

These coordinates can be quantized in the usual manner, using raising and lowering operators [35], but my discussion will be focused purely on classical phenomena.

3.6.1 Special Cases

In the case of a single trapped ion, only the first term in Eq. 3.15 contributes to the system's potential energy and our system is a simple harmonic oscillator. In this case, $u_0 = m{\Omega_0}^2$, where Ω_0 is the frequency of oscillation experienced by the ion in the trap. The experimentally determined value of Ω_0 allows us to understand the parameters of the two-ion system. Specifically, it allows us to both predict the axial resonances for our specific trap and express these resonances relative to the single-ion resonance.

Our experiments are primarily concerned with the trap dynamics resulting from two trapped ions, the staple setup of QLS. Eventually, we hope to trap

an oxygen molecular ion alongside a beryllium ion and use our understanding of beryllium's motion to prepare specific states in the oxygen molecule, but even as we prepare for this step, we can test our system and confirm our theories by trapping two beryllium ions in the trap and observing their resonant frequencies. Furthermore, we often notice one of the beryllium ions disappearing from our view, even as the motion of other visible ions indicate that the now-dark ion is still present, an indication that this ion may have changed mass and therefore is no longer resonant with our laser. Figure 3.7 displays a typical photograph of this scenario. We hypothesize that these dark ions are the result of $^9Be^+$ ions bonding with hydrogen in the trap to form beryllium hydride (BeH^+), which accounts for the changes we observe. In order to confirm the identity of these dark trapped ions, we also need to understand the dynamics of the two-ion case.

Solving Eq. 3.19 for the case of two identical ions yields two normal modes, one in which the two ions oscillate with equal amplitudes and in phase (the center of mass mode), the other in which they oscillate with equal amplitudes but are exactly out of phase (the relative mode). These frequencies differ by a factor of $\sqrt{3}$.

The axial modes of a system containing two ions of different masses can also be obtained from Eq. 3.19. Expressed in terms of the relative masses of the two ions and the single ion resonant frequency, the axial modes are [35]

$$\Omega_{\pm}{}^2 = \Omega_0{}^2\left(1 + \frac{1}{\mu} \pm \sqrt{1 + \frac{1}{\mu^2} - \frac{1}{\mu}}\right), \tag{3.21}$$

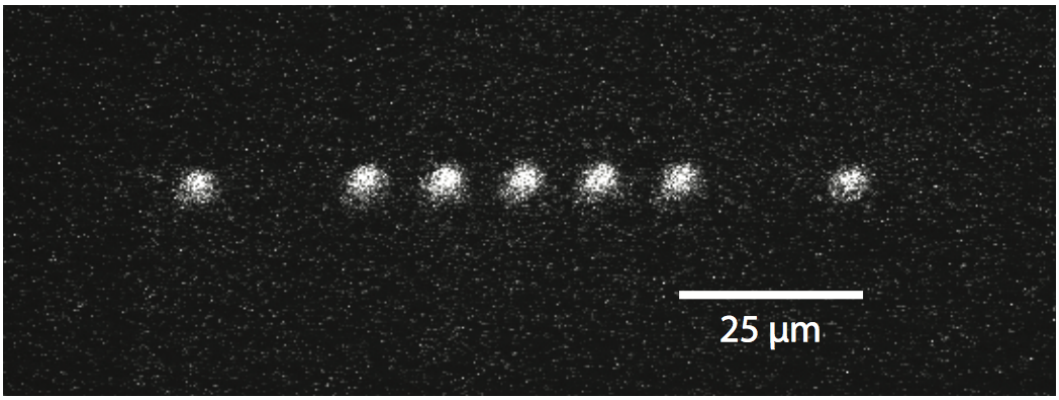

Figure 3.7: Photograph of an Ion Chain with $^{9}Be^{+}$ and Dark Ions. We published this image in Ref. [11]. It shows an ion chain with uneven spacing between the bright beryllium ions. All trapped ions have the same net charge, so they should appear evenly spaced in the presence of the trapping potential. The spacing of the bright ions above indicates the presence of additional trapped ions of a different mass (and thus resonance) in the chain. We think these are BeH^{+} molecular ions created by $^{9}Be^{+}$ bonding with background hydrogen gas in the trap.

where μ is the mass ratio of the two trapped ions of masses M and m such that $M = \mu m$ and $\mu \geq 1$. These modes, relative to the single ion resonant frequency Ω_0, are shown in Fig. 3.8. Notice that when $\mu = 1$, the two ions have equal masses and Ω_- is the center of mass mode, which is greater than the relative mode Ω_+ by a factor of $\sqrt{3}$.

When $\mu \neq 1$, the two normal modes still result in the ions moving either perfectly in or out of phase, but the modes do not exactly correspond to the center of mass and relative modes since the amplitudes are proportional to $1/\sqrt{m}$ [35]. Our three cases of interest are marked in Fig. 3.8: when two $^{9}Be^{+}$ ions are trapped (marked by the vertical axis of the graph), and when one $^{9}Be^{+}$ ion is trapped with either BeH^{+} or $^{16}O_2{}^{+}$ (cases marked by the vertical

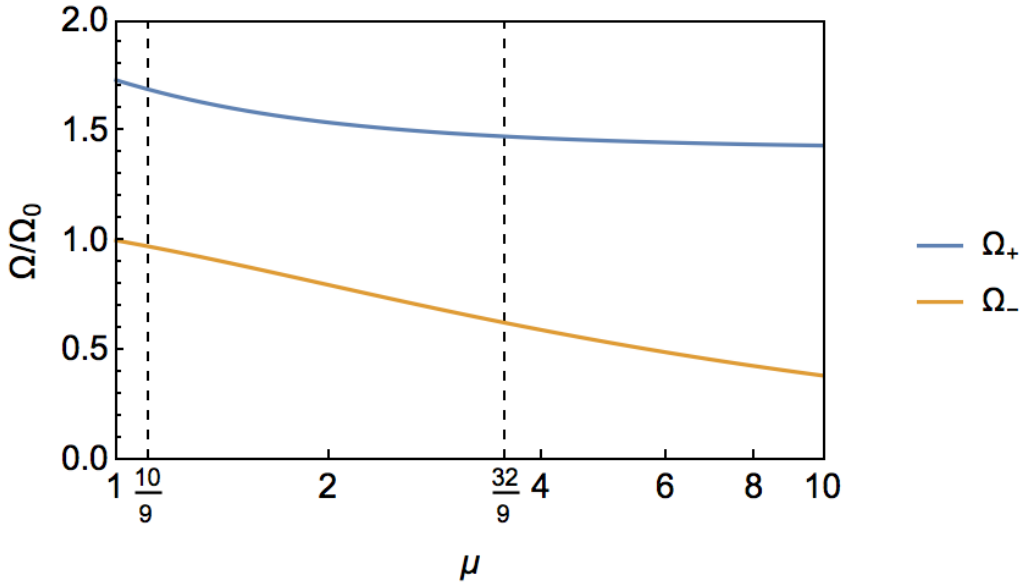

Figure 3.8: Two-ion center of mass and relative mode frequencies. These frequencies are dependent on the mass ratio μ of the two trapped ions. Here they displayed relative to the single ion resonant frequency Ω_0. From left to right, the dashed vertical lines represent the mass ratios for the $^9Be^+$ and BeH^+ system and for the $^9Be^+$ and $^{16}O_2{}^+$ system respectively. The system comprised of two $^9Be^+$ ions is represented by the $\mu = 1$ case, along the vertical axis.

dashed lines).

We test the validity of this framework by searching for the Ω_- and Ω_+ resonances of the $^9Be^+ - ^9Be^+$ system. After touching up the coupling of our RF signal and confirming the presence of two $^9Be^+$ atoms in the trap with the camera, we scanned in 500 Hz steps and found one axial resonance at 239 ± 3 kHz. We increased the drive amplitude, which revealed another axial resonance at 425 ± 2 kHz. Both of these resonances were broad and asymmetric in the scans we took, so these values should be treated only as preliminary measurements.

These modes are separated by a ratio of 1.78. This is approximately the ratio of $\sqrt{3}$ by which we expect the center of mass and relative modes to be separated and thus is consistent with the theory described above. The deviation from the expected value of the ratio indicates that the precision to which our system can identify resonances is limited to a few kHz.

3.7 Two-Ion Resonances

Equation 3.21 allows us to identify co-trapped ions based on the resonances of the two-ion system. This will help us accomplish two important goals. Most importantly, when we load $^{16}{O_2}^+$ into the trap, we will be able to distinguish it from other dark ions based on the frequencies of the system's axial modes. Secondly, it allows us to confirm the identity of the dark ions that have been appearing in our trap.

The phenomenon of a $^9Be^+$ ion interacting with a H_2 molecule to create BeH^+ is a well-documented occurrence in trapping experiments of this kind [6]. While it is important to experimentally confirm the identity of the dark ions co-trapped with $^9Be^+$ in our trap, the purpose of measuring the resonances of the $^9Be^+ - BeH^+$ system is to determine the precision with which we can determine the mass of trapped ions. The normal modes of this system should occur at only slightly lower frequencies than those of the $^9Be^+ - ^9Be^+$ system, since the difference in mass between these two systems is 1 amu. If we can successfully distinguish this case from the $^9Be^+ - ^9Be^+$ case, we can conclude that our system is capable of identifying co-trapped molecules with a precision de-

termined by the difference in resonant frequencies between these two systems.[2] When the system is ready to be loaded with $^{16}O_2{}^+$, we can use this method to confidently identify the presence of co-trapped oxygen and distinguish it from BeH^+.

If we measure an axial resonance of the single trapped $^9Be^+$ system at Ω_0 for a particular trapping potential, we can use Eq. 3.21 to determine the axial modes of the systems of interest to us. This experiment should be feasible with our current setup, but we were unable to collect convincing data as of the writing of this document. In lieu of this data, I will predict the frequency precision which we would need our setup to achieve in order to identify co-trapped BeH^+ or $^{16}O_2{}^+$. For purposes of this discussion, I assume that $\Omega_0 = 300$ kHz with the understanding that this resonance can be tweaked by adjusting U_0.

The mass ratio of BeH^+ to $^9Be^+$ is $\mu = 1.11$. Therefore, if $\Omega_0 = 300$ kHz, the $^9Be^+ - BeH^+$ system should have axial modes at $\Omega_- = 291$ kHz and $\Omega_+ = 507$ kHz. To distinguish both of these modes from those of the $^9Be^+ - ^9Be^+$ system, we need a precision of 9 kHz. It should be easier, however, to focus on the Ω_+ modes due to their higher frequency magnitudes. If we restrict our focus to these modes, a precision of 13 kHz should be sufficient to distinguish these systems. This precision is consistently achieved by our system.

Likewise, we hope to be able to distinguish the $^9Be^+ - ^{16}O_2{}^+$ system ($\mu = 32/9$) from a system with a mass ratio of 33/9 or 34/9, corresponding to a system with a co-trapped oxygen molecule that contains one of oxygen's other

[2]While it is tempting to claim that this experiment confirms that our system can identify co-trapped molecules with a precision of 1 amu, this is not an accurate statement, since a difference of 1 amu causes a larger shift in resonances in systems with lower μ. This can be confirmed with Eq. 3.21.

stable isotopes (^{17}O or ^{18}O). This will allow us to confidently identify the isotope of oxygen we have co-trapped. If $\Omega_0 = 300$ kHz, the $^{9}Be^{+}-^{16}O_2{}^{+}$ system should have axial modes at $\Omega_- = 187$ kHz and $\Omega_+ = 442$ kHz. To distinguish the relative mode of this system from those of similar mass, we need a precision of approximately 0.6 kHz. Currently, we are unable to distinguish such fine detail. A few concepts can help us mitigate this technical limitation.

First, we can increase U_0 to raise Ω_0. If the precision of our measurement is frequency-independent, then increasing Ω_0 lowers the precision necessary to distinguish these systems. We can also rely on the relative abundance of particular oxygen isotopes to help identify trapped $^{16}O_2{}^{+}$. Since ^{16}O is by far the most abundant isotope (with 99.8% abundance), we can assume that we have this isotope trapped. The most important distinction we need to make will certainly be possible with the current precision of our experiment: confirming that the co-trapped dark ion is an oxygen molecule, not a beryllium hydride molecule.

Chapter 4

A Path Forward

There is no clear conclusion to my experimental work. I joined this lab in the middle of an ambitious project, and unfortunately, I will leave it well before we reach our goal. As much as I would like to claim that our lab's precision measurements of the time variation of μ are right around the corner, there is much to still be done before we can make these measurements. With every experiment we perform and every question we answer, new questions arise that merit further investigation. This is not a cause for despair; rather, this is the truly exciting part of navigating to the forefront of physics research. It also means there are many paths forward from the work I've done this year. Instead of attempting to enumerate all of these paths and the many tests on our doorstep, I will focus on those steps which will bring us closer to implementing the quantum toolbox I have assembled for experiments with $^{16}O_2{}^+$.

4.1 Oxygen Loading and Resonances

Of course, before we can begin experimenting on oxygen, we need a reliable way to load and ionize oxygen gas (O_2). We are currently installing an external gas manifold that will allow us to leak a controlled amount of oxygen into our apparatus' vacuum chamber (in which our Paul trap is located) safely and without compromising the vacuum. Specifically, we will leak the gas in at a pressure of approximately 1×10^{-10} torr.

If we simply ionize oxygen ions by striking them with high energy photons, we will generate an ensemble of $^{16}{O_2}^+$ in a large assortment of rotational states. We want to maximally control the quantum states of these molecules for manipulation and cooling, so we need to control which state these molecules are in after being ionized. We will accomplish this by first exciting O_2 gas into a Rydberg electronic state ($d^1\Pi_g$) in a process called resonance-enhanced multiphoton ionization [36, 37]. In a Rydberg state, the electron to be removed in ionization has a large orbit and, therefore, does not dramatically affect the quantum state of the nucleus: The quantum state of an O_2 molecule in a Rydberg state closely resembles a state of the $^{16}{O_2}^+$ ion. This implies that ionizing oxygen gas from this state will yield $^{16}{O_2}^+$ in a known quantum state. As discussed in Refs. [4, 36, 37], exciting oxygen to the $d^1\Pi_g$ Rydberg state requires two photons with wavelengths in the range $296.5 - 303.5$ nm, corresponding to a fundamental wavelength of $593 - 607$ nm. Once the neutral molecule is in this state, we can ionize it with a sufficiently high-energy photon, such as another photon in the UV. We will use a dye laser to create photons of the desired wavelength. These lasers use dyes as a source of optical gain, and

are versatile because a particular dye can be chosen to make the laser function at a desired wavelength. We have preliminarily identified a combination of dyes that could yield the desired wavelength.

Once we have implemented these apparatuses, we can begin studying $^{16}O_2{}^+$ in the trap. An important step at this point will be to confirm that we can sympathetically cool these molecules and trap them alongside $^9Be^+$. Hopefully this step will be straightforward: By simply cooling $^9Be^+$ ions with the detuned beam, we have performed sympathetic cooling of BeH^+ molecules. We expect to be able to cool $^{16}O_2{}^+$ similarly.

The subsequent step, confirming the identity of these cooled ions, will directly use the theory I discussed in Sect. 3.7. By trapping one $^9Be^+$ atom alongside one $^{16}O_2{}^+$ molecule, we can use the mass-dependence of the system's resonant frequencies to confirm that we are, indeed, prepared for quantum logic spectroscopy.

Appendix A

Limitations of BiBO in Second-Harmonic Generation

A.1 The Experiment

In order to prepare the ultraviolet light we use to probe and cool the beryllium in the ion trap, we need to convert infrared light to blue light via second-harmonic generation (SHG). This process involves sending the beam through a nonlinear crystal within a cavity to build power. One of the common crystals used in such setups is bismuth triborate (BiBO, BiB_3O_6). BiBO is particularly useful due to its high nonlinear coefficient which results in a high conversion efficiency in this process [15], but is prone to optical damage induced by photorefraction at high input powers [38]. We have found little documentation in the literature of the symptoms of this damage. In particular, the magnitude and rate of the change in power of the output beam caused by this damage

are not well-catalogued.

The powers involved in our work induced such damage in the BiBO crystal over several thousand seconds of exposure. While we discovered that an LBO crystal was more appropriate for use in our SHG cavity, this provided us with an opportunity to catalog and describe the effects of the BiBO damage on the power of the output beam.

A.1.1 Experimental Setup and Data Acquisition

We sent an infrared beam from a diode laser with a wavelength of 940 nm into our SHG cavity to produce blue light with a wavelength of 470 nm. The diode laser input (controlled by a tapered amplifier and optical fiber coupling) could span a range of powers, capped at approximately 150 mW in the blue. While we witnessed the BiBO damage using input powers as low as 40 mW, we decided to examine the trends resulting from powers between 100 mW and 150 mW to accelerate the decay process.

In order to have a continuous measurement of the output power, we diverted the two beams of blue light deflected out of the SHG cavity, the output and the light reflected off of the BiBO crystal at Brewster's angle, to circuits via photodiodes. These circuits are designed to output a voltage proportional to the input power. By knowing the initial powers of the output and the Brewster-reflected beam, we can determine the circuits' proportionality constants and, thus, convert the measured voltages to powers.

We collected this voltage data with a LabVIEW program which appends voltage samples at a given sample rate to a list. It averages the voltage data

in the list to achieve a mean and an RMS value for that time interval. It appends these data points to a spreadsheet and saves the file after each interval elapses. For this experiment, we set the number of samples to 100 and the sample rate to 1000 per second. Thus, our average voltage data was taken in 100 millisecond intervals.

To acquire data at the instant the BiBO is exposed to damaging levels of light, we first reduced the input laser power to levels well below the damage threshold of the BiBO crystal using a neutral-density (ND) filter. This threshold is difficult to quantify due to its dependence on other systematic factors and acoustic noise [15], but it was sufficiently low that no attenuation of blue power could be seen on timescales of hours in our setup. Next, we translated the crystal position to place the beam on an undamaged area on the BiBO crystal. We began our data acquisition program at this point, then immediately removed the ND filter to instantaneously increase the power. Our graphs all show a dramatic increase in output power when the ND filter was removed, so we can safely omit earlier points from our analysis and consider the moment of the filter's removal as the origin time. We typically acquired several hours worth of data, until significant changes in behavior stopped occurring.

A.2 Features of Output Blue Power Decay

We took a total of eight sets of data, aligning the laser to intersect with an undamaged section of the BiBO crystal between each measurement as described above. Fig. A.1 shows one of the data sets which clearly illustrates the general

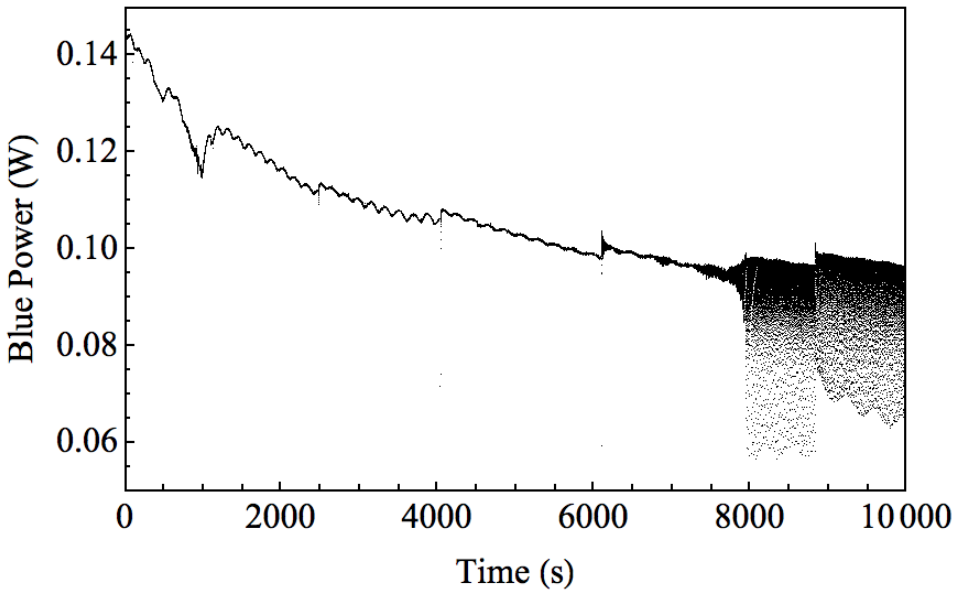

Figure A.1: Symptoms of Photorefractive Damage in BiBO. This graph displays the total blue power generated in the SHG cavity using a BiBO crystal as the crystal is exposed to high-power infrared light over time. Notice the early exponential decay stage followed by the regime of rapid oscillations beginning after approximately 8,000 seconds of exposure.

trends we noticed in most samples. Overall, the decay can be categorized as a combination of exponential decay and oscillations in power. At different points in the decay process, one or the other of these features dominates the behavior of the output power.

When high-power light is incident on an undamaged part of the BiBO crystal, the power decay is dominated by exponential decay. Most of the power's reduction occurs in this regime, with attenuations of 20% to 40% occurring on timescales of 1000s of seconds of exposure. While oscillations in power occur in this regime, their amplitudes are small relative to the overall power, and

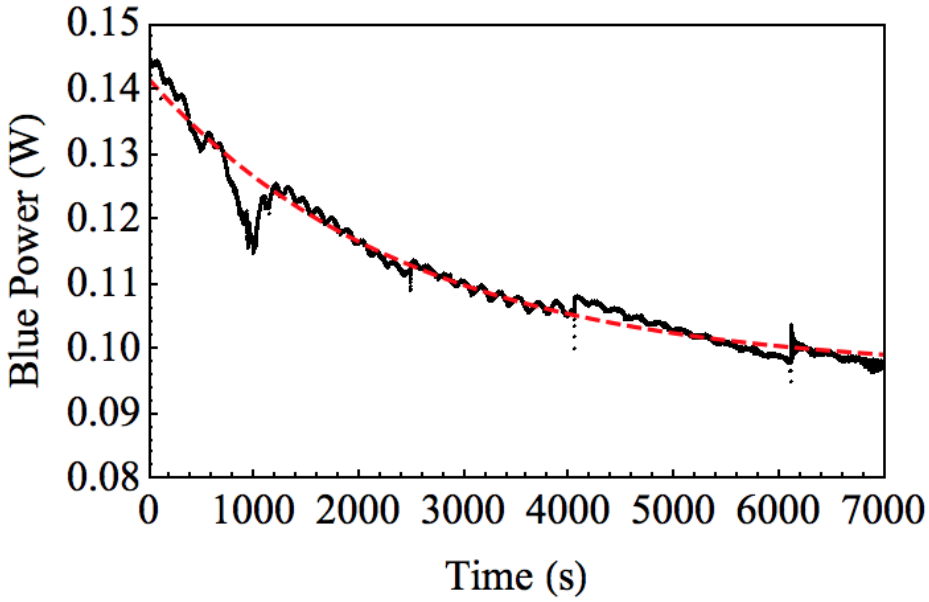

Figure A.2: Symptoms of BiBO Damage in the Decay-Dominated Regime. In the first few thousand seconds of BiBO exposure to high infrared powers, photorefractive damage causes exponential decay in the power of output blue light. The dashed line shows a fit of the data to an exponential curve. Oscillations in this regime are small and have long periods.

their periods are on the order of 100 seconds. Fig. A.2 shows the subset of the data in Fig. A.1 that comprises the decay-dominated regime, where I have fit the data to an exponential curve. While it does not substantially change the features of the regime, it is worth noting that the output power experiences a small increase following a lapse in our signal (typically from the laser unlocking or from acoustic noise shifting the laser's position on the crystal). This behavior can be seen in Fig. A.2 at approximate exposure times of 2,500 seconds, 4,100 seconds, and 6,200 seconds.

In all of our data sets, we witness a transition to the oscillation-dominated

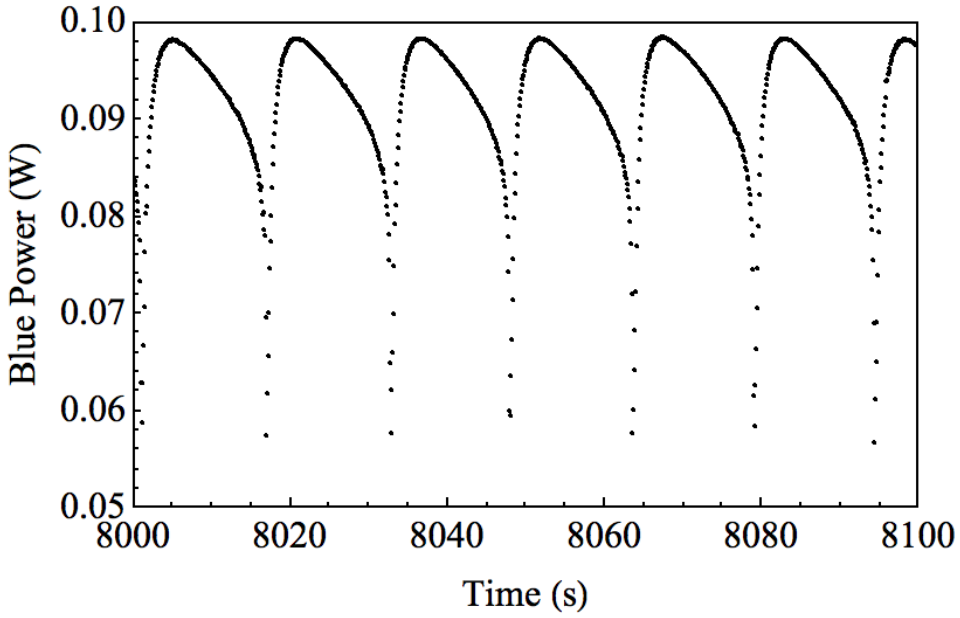

Figure A.3: Symptoms of BiBO Damage in the Oscillation-Dominated Regime. Photorefractive damage caused by exposure of BiBO to high powers of infrared light eventually induce large-amplitude oscillations in output blue power. Exponential decay still occurs, but is not significant in this regime.

regime after a few thousand seconds (in most of our experiments, this occurs after approximately 6,000 seconds of exposure). At this point, the exponential decay that has dominated the output signal has almost reached its asymptote, but the small-scale oscillations in power suddenly become much more pronounced. The periods of these oscillations are markedly smaller than those of the decay-dominated regime, on the order of tens of seconds, and the magnitude of oscillations constitutes a significant fraction of the overall power ($\geq 40\%$). These fast oscillations also exhibit an unusual geometry. The power decreases relatively gradually until it reaches a threshold lower power, at which point it quickly returns to the maximum amplitude. The threshold lower power

is typically consistent over many oscillations, rather than changing after a few cycles. The local peaks of these oscillations still follow the exponential decay pattern of the decay-dominated regime. A local region exhibiting this behavior is shown in Fig. A.3.

Due to the differences between each data set we took, it is difficult to say anything qualitative, let alone quantitative, about the output power decay process beyond the aforementioned properties of the decay. Throughout the data acquisition process, our laser occasionally dropped out, and as we translated the BiBO crystal to expose a new area to damage, we had no definitive means of determining whether this new location on the crystal was, as we assumed, previously undamaged.

Because a reliable data set requires the input laser to remain stable for hours, much of our data is affected by occasional power dropouts. It is unclear what effect these dropouts have on the overall decay process. From Fig. A.1, it appears that the laser dropouts have little effect on the overall behavior of the system, but many of our data sets show that the laser signal dropped out slightly before the transition from the decay-dominated regime to the oscillation-dominated regime, indicating that this sudden change in power triggered the beginning of the oscillation-dominated regime. Similarly, our laser would occasionally drop out during the oscillation-dominated regime, and when the signal returned, the power trend sometimes returned to the decay-dominated regime. The most likely cause for these changes is that when the laser light returned, it was slightly misaligned and therefore incident on a less damaged area of BiBO.

Further investigation into the symptoms of photorefractive damage in BiBO is beyond the scope of this work. However, I hope that my proposed model of two distinct regimes of decay and the general trends I describe here can provide information for a group studying photorefractive damage in more detail.

Appendix B

Constants for Molecules with Hypothetical Sensitivity to μ Variation

Detailed in Table B.1 are homonuclear diatomic molecules that fit criteria which should make them sensitive to variation in the proton-to-electron mass ratio μ. As discussed in Sect. 2.3, these molecules were chosen on the basis of having deep potential wells, a different multiplicity state which overlaps with the ground state, and closely-spaced vibrational energy levels (a result of low constants ω_e and $\omega_e x_e$). Relative sensitivity is maximized if a transition is considered between a state with high sensitivity to μ and a state with low sensitivity to μ. For instance, a transition between a ground electronic state vibrational level with an energy of approximately $.75D_e$ and a higher electronic state near the ground vibrational level should be maximally sensitive. Thus,

the seventh column in this table lists T_e/D_e, the fractional distance up the ground electronic state potential well where the other state's energy minimum is located. Considering a transition between nearly degenerate states in this region should yield a maximum absolute and relative precision in measuring μ variation.

Molecule	State	T_e	ω_e	$\omega_e x_e$	D_e	T_e/D_e
$O_2{}^+$	$\|X^2\Pi_g\rangle$	0	1 904.7[a]	16.5054(84)[b]		
	$\|a^4\Pi_u\rangle$	32 964[a]	1 035.69[a]	10.382(23)[c]	54 600	.60
N_2	$\|X^1\Sigma_g^+\rangle$	0	2 358.57[a]	14.324[a]		
	$\|B^3\Sigma_u^-\rangle$	66 272.4[a]	1 516.88[a]	12.18[a]	97 089	.68
Cl_2	$\|X^1\Sigma_g^+\rangle$	0	559.7[a]	2.67[a]		
	$\|B^3\Pi_u^+\rangle$	17 809[a]	259.5[a]	5.3[a]	29 331	.61
Br_2	$\|X^1\Sigma_g^+\rangle$	0	325.321[a]	1.0774[a]		
	$\|B^3\Pi_u\rangle$	15 902.47[a]	167.607[a]	1.6361[a]	24 558	.65
$I_2{}^+$	$\|X^2\Pi_{3/2,g}\rangle$	0	239.0397(55)[d]	0.64951(87)[d]		
	$\|a^4\Sigma_u^-\rangle$	8 258	128 ± 2[e]	0.38 ± 0.02[e]	15 478	.53

Table B.1: Molecular Constants for Select Molecules. [a]Ref. [21], [b]Ref. [27], [c]Ref. [28], [d]Ref. [26], [e]Ref. [25]. All numbers are in units of cm^{-1}, and uncertainties are marked as they were listed in the source. $T_e = 0$ in the ground states by definition, and D_e is calculated from the ground state values with Eq. 2.6. Refs. [21, 24] include data on many homonuclear diatomic molecules not listed here.

Appendix C

DDS Board Calibrations

Figure C.1 shows calibrations of the DDS board used to perform axial potential modulation for the experiments described in Chapter 3. This data was taken on an oscilloscope with the DDS set to an amplitude of 100% and connected to a 50 Ω terminator. While the signal attenuates at frequencies < 1 MHz, its amplitude is sufficient to drive the axial and radial modes of trapped ions without amplification. To drive axial resonances, we typically operated at an amplitude of 30%. To drive radial resonances, we typically operated at an amplitude of $70 - 100\%$. The typical frequency range of our scans of system resonances, 100 kHz $-$ 800 kHz, is bounded by the dashed lines in Fig. C.1.

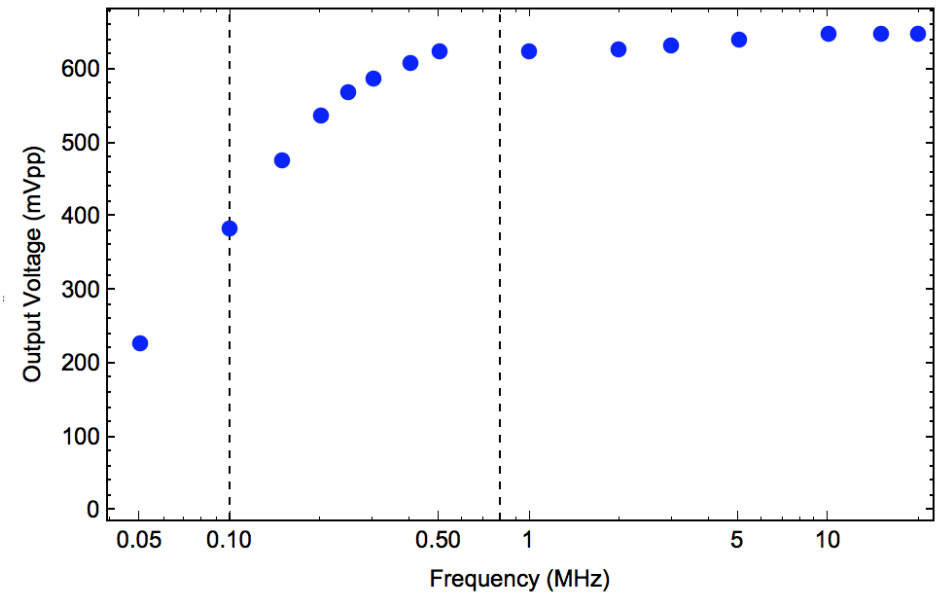

Figure C.1: DDS Output Voltage at 100% Amplitude. The vertical dashed lines represent the typical range of our frequency scans.

Bibliography

[1] P. A. M. Dirac, "A New Basis for Cosmology," Proceedings of the Royal Society A **165**, 199 (1937).

[2] J.-P. Uzan, "The fundamental constants and their variation: observational and theoretical status," Rev. Mod. Phys. **75**, 403 (2003).

[3] D. DeMille, S. Sainis, J. Sage, T. Bergeman, S. Kotochigova, and E. Tiesinga, "Enhanced Sensitivity to Variation of m_e/m_p in Molecular Spectra," Phys. Rev. Lett. **100**, 043202 (2008).

[4] D. Hanneke, R. A. Carollo, and D. A. Lane, "High sensitivity to variation in the proton-to-electron mass ratio in $O_2{}^+$," Phys. Rev. A **94**, 050101 (2016).

[5] P. O. Schmidt, T. Rosenband, W. M. Itano, J. C. Bergquist, and D. J. Wineland, "Spectroscopy Using Quantum Logic," Science **309**, 749 (2005).

[6] D. J. Wineland, C. Monroe, W. M. Itano, D. Liebfried, B. E. King, and D. M. Meekhof, "Experimental Issues in Coherent Quantum-State Ma-

nipulation of Trapped Atomic Ions," J. Res. Natl. Inst. Stand. Technol. **103**, 259 (1998).

[7] H. J. Metcalf and P. van der Straten, *Laser Cooling and Trapping* (Springer, New York, 1999).

[8] E. K. Kleiner, *Quantum Control of Be^+ Ions*, B.A. thesis, Amherst College (2016).

[9] D. J. Wineland, "Trapped Ions, Laser Cooling, and Better Clocks," Science **226**, 395 (1984).

[10] W. Nagourney, *Quantum Electronics for Atomic Physics* (Oxford University Press Inc., New York, 2010).

[11] R. A. Carollo, D. A. Lane, E. K. Kleiner, P. A. Kyaw, C. C. Teng, C. Y. Ou, S. Qiao, and D. Hanneke, "Third-harmonic-generation of a diode laser for quantum control of beryllium ions," Optics Express **25**, 7220 (2017).

[12] F. M. J. Cozijn, J. Biesheuvel, A. S. Flores, W. Ubachs, G. Blume, A. Wicht, K. Paschke, G. Erbert, and J. C. J. Koelemeij, "Laser cooling of beryllium ions using a frequency-doubled 626 nm diode laser," Optical Letters **38**, 2370 (2013).

[13] C. Monroe, D. M. Meekhof, B. E. King, S. R. Jefferts, W. M. Itano, D. J. Wineland, and P. Gould, "Resolved-Sideband Raman Cooling of a Bound Atom to the 3D Zero-Point Energy," Phys. Rev. Lett. **75**, 4011 (1995).

[14] C. C. Teng, *Frequency Control and Stabilization of a Laser System*, B.A. thesis, Amherst College (2013).

[15] V. Ruseva and J. Hald, "Generation of UV light by frequency doubling in BIBO," Optics Communications **236**, 219 (2004).

[16] R. M. Godun, P. B. R. Nisbet-Jones, J. M. Jones, S. A. King, L. A. M. Johnson, H. S. Margolis, K. Szymaniec, S. N. Lea, K. Bongs, and P. Gill, "Frequency Ratio of Two Optical Clock Transitions in $^{171}Yb^{+}$ and Constraints on the Time Variation of Fundamental Constants," Phys. Rev. Lett. **113**, 210801 (2014).

[17] N. Huntemann, B. Lipphardt, C. Tamm, V. Gerginov, S. Weyers, and E. Peik, "Improved Limit on a Temporal Variation of m_p/m_e from Comparisons of Yb^{+} and Cs Atomic Clocks," Phys. Rev. Lett. **113**, 210802 (2014).

[18] K. Beloy, A. Borschevsky, P. Schwerdtfeger, and V. V. Flambaum, "Enhanced sensitivity to the time variation of the fine-structure constant and m_p/m_e in diatomic molecules: A closer examination of silicon monobromide," Phys. Rev. A **82**, 022106 (2010).

[19] C. Chin, V. V. Flambaum, and M. G. Kozlov, "Ultracold molecules: new probes on the variation of fundamental constants," New Journal of Physics **11**, 055048 (2009).

[20] S. Schiller and V. Korobov, "Tests of time independence of the electron and nuclear masses with ultracold molecules," Phys. Rev. A **71**,

032505 (2005), URL https://link.aps.org/doi/10.1103/PhysRevA.71.032505.

[21] K. P. Huber and G. Herzberg, *Molecular Spectra and Molecular Structure*, vol. IV (Van Nostrand Reinhold Company, New York, 1979).

[22] G. Herzberg, *Spectra of Diatomic Molecules* (D. Van Nostrand Company, Inc., New York, 1950).

[23] T. Zelevinsky, S. Kotochigova, and J. Ye, "Precision Test of Mass-Ratio Variations with Lattice-Confined Ultracold Molecules," Phys. Rev. Lett. **100**, 043201 (2008).

[24] K. Balasubramanian, "Spectroscopic Constants and Potential Energy Curves of Heavy p-Block Dimers and Trimers," Chem. Rev. **90**, 93 (1990).

[25] M. C. R. Cockett, R. J. Donovan, and K. P. Lawley, "Zero kinetic energy pulsed field ionization (ZEKE-PFI) spectroscopy of electronically and vibrationally excited states of I_2^+: The $A^2_{\Pi 3/2,u}$ state and a new electronic state, the $a4^-_{\Sigma u}$ state," The Journal of Chemical Physics **105**, 3347 (1996).

[26] L. hua Deng, Y. yue Zhu, C. liang Li, and Y. qin Chen, "High-resolution observation and analysis of the I_2^+ $A^2\Pi_{3/2,u}$-$X\,2\Pi_{3/2,g}$ system," The Journal of Chemical Physics **137**, 054308 (2012).

[27] W. Kong and J. W. Hepburn, "Rotationally resolved threshold photoelectron spectroscopy of O_2 using coherent XUV: formation of vibrationally excited ions in the Franck-Condon gap," Can. J. Phys. **72**, 1284 (1994).

[28] J. C. Hansen, J. T. Moseley, and P. C. Cosby, "High-resolution photofragment spectroscopy of the O_2^+ $b^4\Sigma_g^-$ $(v' = 5-8) \leftarrow a^4\Pi_u$ $(v'' = 6-9)$ first negative system," Journal of Molecular Spectroscopy **98**, 48 (1983).

[29] D. J. Griffiths, *Introduction to Electrodynamics* (Pearson, 2013), 4th ed.

[30] S. Qiao, *Constructing a Linear Paul Trap System for Measuring Time-variation of the Electron-Proton Mass Ratio*, B.A. thesis, Amherst College (2013).

[31] W. Paul, "Electromagnetic traps for charged and neutral particles," Reviews of Modern Physics **62**, 531 (1990).

[32] M. Raizen, J. Gilligan, J. Bergquist, W. Itano, and D. Wineland, "Ionic crystals in a linear Paul trap," Physical Review A **45**, 6493 (1992).

[33] M. Drewsen and A. Brøner, "Harmonic linear Paul trap: Stability diagram and effective potentials," Physical Review A **62**, 045401 (2000).

[34] J. P. Home, D. Hanneke, J. D. Jost, D. Leibfried, and D. J. Wineland, "Normal modes of trapped ions in the presence of anharmonic trap potentials," New Journal of Physics **13**, 073026 (2011).

[35] G. Morigi and H. Walther, "Two-species Coulomb chains for quantum information," The European Physical Journal D **13**, 261 (2001).

[36] A. Dochain and X. Urbain, "Production of a rovibrationally selected O_2^+ beam for dissociative recombination studies," EPJ Web Conf. **84**, 05001 (2015).

[37] A. Sur, R. S. Friedman, and P. J. Miller, "Rotational dependence of the Rydberg-valence interactions in the $^1\Pi_g$ states of molecular oxygen," The Journal of Chemical Physics **94**, 1705 (1991).

[38] J. H. Jang, I. H. Yoon, and C. S. Yoon, "Cause and repair of optical damage in nonlinear optical crystals of BiB3O6," Optical Materials **31**, 781 (2009).